Chapter 5
Topochemistry of Spatially Extended sp^2 Nanocarbons: Fullerenes, Nanotubes, and Graphene

Elena F. Sheka

Abstract This chapter presents sp^2 nanocarbons as a new class of topochemical species from the insight of the computational study of peculiar properties that accompany the formation of different composite, at least, one member of that is a sp^2 nanocarbon. The composites, which are resulted from either the "double-(C–C)-bond" reactions between two sp^2 nanocarbons or the "atom-(C–C)-bond" reactions, concerned with a monatomic species deposition on the nanocarbons, manifest clearly seen properties that can be addressed to the action of either internal or external topology. The internal topology is attributed to the inherited properties of each nanocarbon while the external topology is related to external factors that drastically influence the chemical reactions involving nanocarbons.

5.1 Introduction

The modern topology in chemistry covers two large valleys, namely, formal, mathematical and empirical, chemical. The former is concerned with the description of molecular structures on the basis of finite topological spaces. The space shows itself as a mathematical image or instrument of theoretical study. A large collection of comprehensive reviews, related to a topological description of fullerenes from this viewpoint, has recently been published (Cataldo et al. 2011). The second field covers vastly studied topochemical reactions. The space in this case is a physical reality defining the real place where the reactions occur. If the appearance of mathematical topology in chemistry can be counted off the publication of the Merrifield and Simmons monograph in 1989 (Merrifield and Simmons 1989), topochemical reactions have been studying from the nineteenth century (see Schmidt 1971 and

---

E.F. Sheka (✉)
Peoples Friendship University of Russia, 117198 Moscow, Russia
e-mail: sheka@icp.ac.ru

A.R. Ashrafi et al. (eds.), *Topological Modelling of Nanostructures and Extended Systems*, Carbon Materials: Chemistry and Physics 7, DOI 10.1007/978-94-007-6413-2_5,

references therein). The first stage of the study was completed in the late 1920s (de Jong 1923) and then obtained a new pulse after appearing the Woodward and Hoffmann monograph, devoted to the conservation of orbital symmetry, in 1970 (Woodward and Hoffmann 1970). Since then, topochemical reactions have become an inherent part of not only organic but inorganic chemistry, as well. The readers, who are interested in this topic, are referred to a set of comprehensive reviews (Schmidt 1971; Enkelmann 1984; Hasegawa 1986; Boldyrev 1990; MacGillivray and Papaefstathiou 2004), but a few. The current situation in this field can be seen by the example of a direct structural understanding of a topochemical solid-state photopolymerization reaction (Guo et al. 2008).

Nowadays, we are witnessing the next pulse, stimulating investigations in the field, that should be attributed to the appearance of a new class of spatially extended molecular materials, such as sp^2 nanocarbons. Obviously, the main members of the class such as fullerenes, nanotubes, and numerous graphene-based species are absolutely different from the formal topology viewpoint. Thus, fullerenes exist in the form of a hollow sphere, ellipsoid, or tube consisting of differently packed benzenoid units. Carbon nanotubes present predominantly cylindrical packing of the units. In graphene, the benzenoid units form one-atom-thick planar honeycomb structure. If we address the common terms of the formal topology, namely, the connectivity and adjacency, we have to intuitively accept their different amount in the above three species. In its turn, the connectivity and adjacency determine the "quality" of the C–C bond structure of the species, thus, differentiating them by this mark. Since non-saturated C–C bonds are the main target for chemical reactions of any type, one must assume that identical reactions, involving the bonds, will occur differently for different members of the sp^2 nanocarbon family. Therefore, one may conclude that the spatially extended sp^2 nanocarbons present not only peculiarly structural chemicals but the class of species for which the formal and empirical topology overlap. The results presented in this chapter are aimed at revealing this tight interconnection in terms of molecular quantum theory. Not only fullerenes but carbon nanotubes and graphene (their fragments) are considered at the molecular level. The obtained results are related to the computational study of the intermolecular interaction (IMI) between one of the above sp^2 nanocarbon molecules and one of the other addends, among which there are both sp^2 nanocarbons and monatomic species. The intermolecular interaction lays the foundation of any reaction, so that its topological peculiarities may evidence a topochemical character of the reaction under study.

This chapter is organized as follows. Section 5.2 presents main concepts that form the grounds of the IMI consideration as well as introduces terms and quantities in use. Section 5.3 is devoted to the IMI investigation in the $(C_{60})_n$ composites related to the dimerization and oligomerization of fullerene C_{60}. The IMI peculiarities, characteristic for composites fullerene-carbon nanotube (C_{60} + CNT) and fullerene-nanographene (NGr) (C_{60} + NGr), are considered in Sects. 5.4 and 5.5, respectively. Section 5.6 summarizes conclusive remarks about [2 + 2] cycloadditions that present a typical contact zone for the three types of the studied composites. Section 5.7 is devoted to carbon nanotube-nanographene (CNT + NGr) composites.

Section 5.8 presents a comparative study of the topochemical behavior of the hydrogenation of fullerene C_{60} and nanographene. Topological view on the graphene deformation is discussed in Sect. 5.9. General conclusion is presented in Sect. 5.10.

5.2 Odd Electrons and Donor–Acceptor Ability as Leitmotifs of Intermolecular Interaction in sp^2 Nanocarbons

Two cornerstones lay the foundation of the electronic properties of sp^2 nanocarbon molecules. The first concerns odd-electron nature of their atomic system, aggravated with the correlation of these electrons and is intramolecular by nature. The second is provided with extremely high donor and acceptor characteristics of these molecules and is intimately connected with intermolecular interaction that is smoothly transformed into peculiar intramolecular properties of the species derivatives and composites. While, on the subject of covalent bonding, which involves any of sp^2 nanocarbons, we should always proceed from the molecule partial radicalization due to exceeding C–C bond length the critical value $R_{\text{cov}}^{\text{crit}}$ 1.395 Å under which the odd electrons are non-correlated and fully covalently bound-forming classical π electron pairs and over which those become correlated and effectively unpaired (Sheka 2011a, 2012). Thus, appeared effectively unpaired electrons form a pool of molecular chemical susceptibility determined by the total number of the unpaired electrons N_D. Distributed over the molecule atoms by partial number N_{DA}, the electrons highlight the map of its chemical activity in terms of atomic chemical susceptibility (ACS) N_{DA}. The atom with the highest ACS first enters the reaction.

The second fundamental property concerns IMI. In all cases, the IMI is greatly contributed with the donor–acceptor (DA) interaction since all the sp^2 nanocarbons are simultaneously good donors and acceptors of electron (Sheka 2004, 2007a, 2011a). Within the framework of general characteristics of the DA interaction, the IMI term configuration in the ground state depends on the difference of the asymptotes, $E_{\text{gap}} = I_A - \varepsilon_B$, of the $E_{\text{int}}(A^+B^-)$ and $E_{\text{int}}(A^0B^0)$ terms that describe the interaction between molecular ions and neutral molecule, respectively. Here, I_A and ε_B present ionization potential and electron affinity of components A and B. When E_{gap} is as big as in the case of C_{60} dimers, the IMI term of the ground state has a typical two-well shape (Sheka 2007a) shown in Fig. 5.1. The formation of a stationary product AB at the point R^{+-} is accompanied by the creation of “intermolecular” chemical bonds between A and B partners. Oppositely, quite widely spaced neutral moieties form a charge transfer complex $A + B$ in the vicinity of R^{00} (Sheka 2004, 2007a, 2011a). In spite of the formation of AB product is energetically profitable, the yield of the relevant reaction, which starts from $A + B$ mixture at all time, is determined by a barrier that separates $A + B$ and AB products. This chapter in its main part is focused on the determination (1) how similar are the IMI profiles for three types of composites, namely, $C_{60} + C_{60}$, C_{60} + CNT, and C_{60} + NGr, that include C_{60} as a permanent component while the other component

Fig. 5.1 Scheme of terms of an IMI potential of type 1 (Sheka 2011a). (A^0B^0) and (A^+B^-) match the term branches related to the IMI between neutral molecules and their ions, respectively

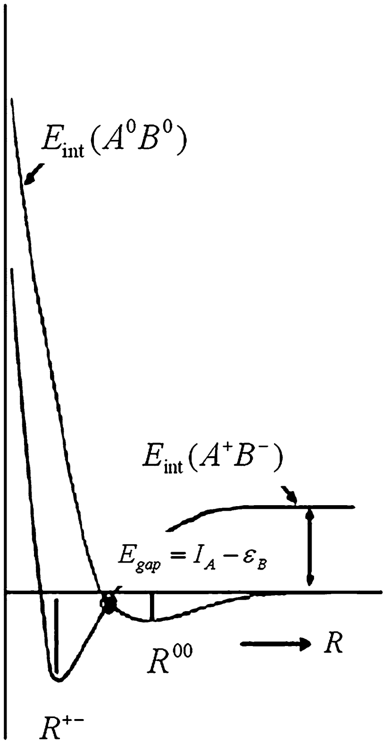

is either C_{60} or CNT and NGr and (2) how big is the barrier of the *AB* product formation in each case. In the abbreviated form, the problem will be discussed as regards CNT + NGr composites, as well.

It should be noted that the above-mentioned composites are similar to those that are formed by non-saturated organic moieties, whose topochemical [2 + 2] photocyclo-dimerization-polymerization in solid state has been the main subject of a quite exhausted studying for many years (see Schmidt 1971; Enkelmann 1984; Hasegawa 1986; Guo et al. 2008), but a few. However, until now these topochemical reactions have not been considered from the position of the IMI complication caused by the donor–acceptor interaction. Starting from the monograph of Woodward and Hoffmann (1970), all the explanations have been concentrated on the consideration of the formation of chemically bound *AB* products. As will be shown in what follows, the consideration of the composite properties at the platform of the DA-complicated IMI opens much larger perspectives to enter the depth of the considered phenomenon.

This chapter presents the view of the touched problems from the insight of quantum-chemical calculations. The main part of the results was obtained by computations carried out by the author team when using the AM1 semiempirical version of unrestricted broken symmetry Hartree-Fock (UBS HF) approach (Sheka 2011a, 2012).

5.3 Fullerene + Fullerene Composites

5.3.1 Ground State Term of the $C_{60} + C_{60}$ Dyad. Equilibrium Structure and Mechanism of Dimerization

According to the scheme in Fig. 5.1, the reaction of the $(C_{60})_2$ dimer formation can be considered as moving the two molecules towards each other, once spaced initially at large intermolecular distance R, then equilibrated and coupled as A + B complex in the R^{00} minimum and afterwards achieved the minimum at R^{+-} to form tightly bound adduct AB. The last stage implies overcoming a barrier, which is followed by the transition from $\left(A^0B^0\right)$ to $\left(A^+B^-\right)$ branch of terms after which the Coulomb interaction between molecular ions completes the formation of the final AB adduct at the R^{+-} minimum.

Concerning covalent bonding, which involves fullerene C_{60}, we should usually begin from the map of chemical activity of C_{60} in terms of atomic chemical susceptibility (ACS) N_{DA} (Sheka and Zayetz 2005; Sheka 2007b). Plottings of the ACS distribution over atoms of the C_{60} molecule are shown in Fig. 5.2 and are emphasized by different colors in the insert that distinguish atoms with different ACS. Among the latter, the most active atoms are shown by light gray. Those are the first targets involved into initial stages of any addition reaction. Following this indication, the initial composition of a pair of the C_{60} molecules shown in Fig. 5.3a becomes quite evident. The starting configuration corresponds to R^{st}_{CC} 1.7 Å that corresponds to the distances between 1–1′ and 2–2′ target atoms. A bound dumbbell-like dimer is formed (Fig. 5.3b) after the structure optimization aimed at the total energy minimization is completed. It turns out that two monomers within the dimer are contacted via a typical [2 + 2] cycloaddition of “66” bonds that form a cyclobutane ring (Sheka 2007a). Main electronic characteristics of the $(C_{60})_2$ adduct are presented in Table 5.1. A detailed comparison with the available computational data is given elsewhere (Sheka 2007a). A large negative E^{tot}_{cpl} value undoubtedly evidences that $(C_{60})_2$ dimer is a typical AB adduct attributed to the R^{+-} minimum on the IMI ground state term in Fig. 5.1.

When $R^{st}_{CC} = 3.07$ Å, optimization of the initial structure leads to the formation of a weakly bound pair of molecules spaced by $R^{fin}_{CC} = 4.48$ Å. Monomer molecules preserve their initial configurations and, as seen from Table 5.1, form a classical charge transfer complex. The fragment composition of the HOMO and LUMO is cross-partitioned; the former should be attributed to Mol 2 while the latter to Mol 1, just showing that a charge transfer from Mol 2 to Mol 1 occurs when the complex is photoexcited.

The obtained results allow for highlighting mechanisms of C_{60} dimerization. Since the IMI interaction in the C_{60} pair is described by two-well terms shown in Fig. 5.1, at ambient conditions, the dimerization does not occur spontaneously which points to the reaction barrier. According to experimental findings, the barrier (activation energy) is 1.25 eV (Wang et al. 1994) in the case of photostimulated dimerization and 1.40 eV (Davydov et al. 2001) when high pressure is applied.

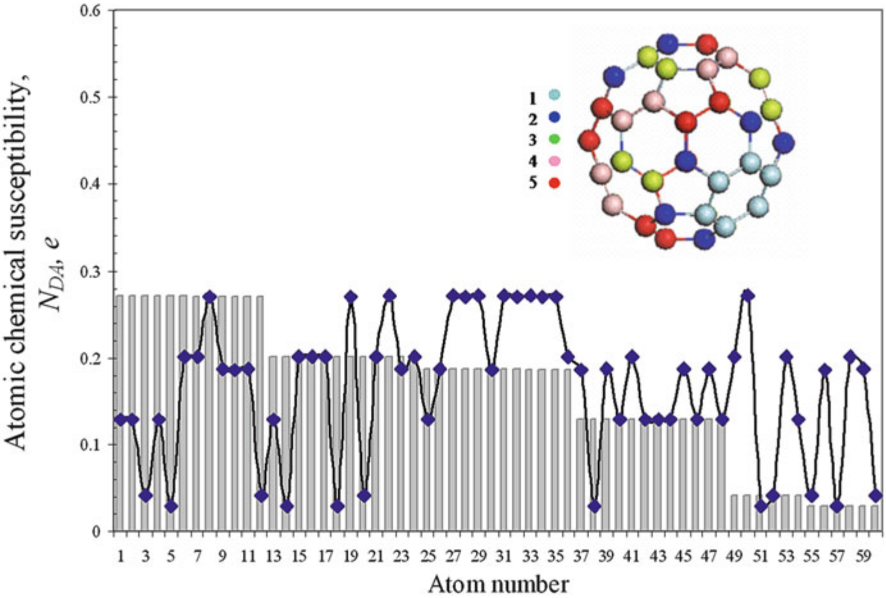

Fig. 5.2 Atomic chemical susceptibility of fullerene C_{60} (Sheka 2011a), distributed over the molecule atoms according to either their numeration in the output file (*curve* with *rhombs*) or in the Z → A manner (histogram). Different colors in the insert distinguish five atomic groups shown by the histogram

Fig. 5.3 (**a**) Starting composition of the $C_{60} + C_{60}$ dyad. (**b**) Equilibrium structure of the $(C_{60})_2$ dimer; $R_{CC}^{st} = 1.7$ Å, $R_{CC}^{fin} = 1.55$ Å. Both distances correspond to spacings between 1–1′ and 2–2′ atoms

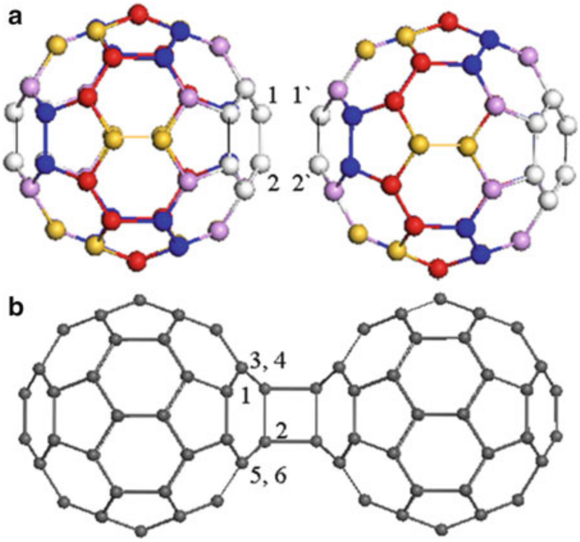

Table 5.1 Electronic characteristics of the $C_{60} + C_{60}$ dyad

Computed quantities,		R^{st}_{CC}	
UBS HF AM1 singlet state	Monomer C_{60}	1.71 Å	3.07 Å
Heat of formation[1], ΔH, kcal/mol	955.56	1,868.49	1,910.60
Coupling energy[2], E^{tot}_{cpl}, kcal/mol	–	−42.63	−0.52
Ionization potential[3], I, eV	9.86 (8.74[a])	9.87	9.87
Electron affinity[3], ε, eV	2.66 (2.69[b])	2.62	2.66
Dipole moment, *Db*	0.01	0.001	0.001
Squared spin, $(S^{**}2)$	4.92	10.96	9.87
Total number of effectively unpaired electrons, N_D[4]	9.84	21.93	19.75
Gained charge to Mol 1	–	0.0	0.0
Transferred charge from Mol 2	–	0.0	0.0
Symmetry	C_i	C_{2h}	C_i
HOMO, fragment compositions, η	–	$\eta_{Mol1} = 61.8\ \%$	$\eta_{Mol1} = 0\ \%$
		$\eta_{Mol2} = 38.1\ \%$	$\eta_{Mol2} = 100\ \%$
LUMO, fragment compositions, η	–	$\eta_{Mol1} = 83.9\ \%$	$\eta_{Mol1} = 100\ \%$
		$\eta_{Mol2} = 15.8\ \%$	$\eta_{Mol2} = 0\ \%$

Reprinted from Sheka (2007a). Copyright (2007) with permission from Elsevier

[1] Molecular energies are heats of formation ΔH determined as $\Delta H = E_{tot} - \sum_A \left(E^A_{elec} + E\ \mathrm{HEAT}^A\right)$. Here $E_{tot} = E_{elec} + E_{nuc}$, while E_{elec} and E_{nuc} are the electron and core energies. E^A_{elec} and $E\mathrm{HEAT}^A$ are electron energy and heat of formation of an isolated atom, respectively

[2] Coupling energy is determined by Eq. (5.1)

[3] Here I and ε correspond to the energies of HOMO and LUMO, respectively, just inverted by sign. Experimental data for the relevant orbitals are taken from Weaver et al. (1991)[a] and Wang et al. (1999)[b]

[4] The total number of effectively unpaired electrons, N_D, displays the molecular chemical susceptibility of the species (Sheka and Zayetz 2005; Sheka 2007b)

The barrier can be overcome by different ways, which describes a large variety of the technological schemes in use. Among the latter, there are thermal and high pressure technologies (Yamawaki et al. 1993; Pekker et al. 1994; Iwasa et al. 1994), field-stimulated dimer formation and decomposition (Zhao et al. 1994; Nakaya et al. 2008), but the first place is taken by the photoexcitation technology (Ecklund et al. 1995).

A triplet state photochemical mechanism is usually accepted, according to which one monomer in the excited triplet state $^3M^*$ reacts with the other monomer in the ground state M to yield the dimer D, that is, $^3M^* + M \rightarrow D$. This view on the mechanism of the photopolymerization has come from those topochemical reactions that were discussed earlier. However, another mechanism seems to be more efficient. As shown above, two C_{60} molecules separated by ~4.5 Å form a charge transfer complex at the point R^{00} (Sheka et al. 2007). In solid C_{60}, photostimulated charge transfer between adjacent molecules causes the appearance of charge transfer excitons (Pac et al. 1998; Kazaoui et al. 1998). The related absorption bands, both in molecular solutions and solids, are provided by phototransitions out of minimum R^{00} belonging to the term $E_{int}(A^0B^0)$ to the branch of the term $E_{int}(A^+B^-)$

(see Fig. 5.1) in due course of which the ground state of weakly interacting neutral molecules is transformed into the charge transfer state of molecular ions. By this means, photoexcitation of a van der Waals C_{60} pair by visible-UV light is followed by the formation of the ion pair located above the barrier. Coulomb's interaction between the ions provides their passing towards the R^{+-} minimum where the dimer is formed.

This mechanism may explain a severe requirement, known for more than a century, for solid-state photostimulated reactions: the molecular moieties should be spaced not more than 4.2–4.7 Å for the topochemical photodimerization-oligomerization to occur (Schmidt 1971; Enkelmann 1984; Friscicґ and MacGillivray 2005). The distance is characteristic for R^{00} that determines the equilibrium spacing in charge transfer complexes. If the formation of the charge transfer complex provides this photoreaction, the encountered molecules should be simultaneously donors and acceptors of electrons. During the preparation of this chapter, the author has proven the "4.2–4.7" rule for such typical representatives of the discussed topochemical reactants as α-cinnamic acid and *n*-diethynilbenzene. As turned out, they both are good donors and acceptors of electrons, indeed.

5.3.2 The Barrier for the Formation and/or Decomposition of $(C_{60})_2$ Dimer

To get the barrier profile of the reaction under consideration, it is necessary not only to determine equilibrium configurations $A + B$ and AB but to trace a continuous transition from one state to the other. Computationally, it is no difference to study the profile by either shifting monomer molecules of the $A + B$ complex towards each other, thus contracting the corresponding intermolecular C–C distances and determining the barrier of the C_{60} dimerization or separating the molecules of the AB product by elongation of the relevant intermolecular C–C bonds and thus getting the barrier of the dimer decomposition. In contrast to the equilibrium configuration $A + B$, which does not critically depend on mutual orientation of the partners, a particular combination of the partners' atoms constructs the contact zone of the AB product (see Fig. 5.3a). Since that, the determination of the decomposition barrier is more structurally substantiated. The procedure involves a regular elongation of the relevant intermolecular bonds of the equilibrium AB structure. These bonds are kept fixed at each elongation step while C_{60} molecules relax in looking for the total energy minimum. According to this, two intermolecular C–C distances, namely, 1–1′ and 2–2′ separations of the $[2 + 2]$ cycloaddition in Fig. 5.3b, are gradually elongated with a constant increment of 0.05 Å during the first stage of elongation from 1.57 to 2.22 Å and then of 0.1 Å during the second stage. Figure 5.4 presents a profile of thus obtained barrier for the dimer $(C_{60})_2$ decomposition presented by the total coupling energy $E^{\mathrm{tot}}_{\mathrm{cpl}}$ determined as

$$E^{\mathrm{tot}}_{\mathrm{cpl}}(R_{\mathrm{CC}}) = \Delta H_{\mathrm{dim}}(R_{\mathrm{CC}}) - 2\Delta H^{\mathrm{eq}}_{\mathrm{mon}}, \tag{5.1}$$

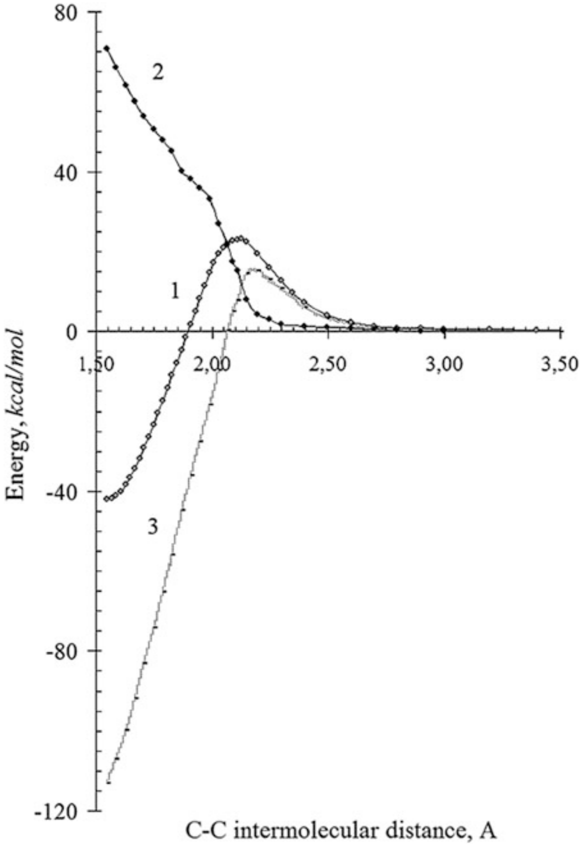

Fig. 5.4 Profile of the barrier of the dimer $(C_{60})_2$ decomposition (Reproduced from Sheka and Shaymardanova (2011b), with permission from the Royal Society of Chemistry). *1.* $E^{\mathrm{tot}}_{\mathrm{cpl}}(R_{\mathrm{CC}})$; *2.* $E^{\mathrm{tot}}_{\mathrm{def}}(R_{\mathrm{CC}})$; *3.* $E^{\mathrm{tot}}_{\mathrm{chem}}(R_{\mathrm{CC}})$ (see text)

where $\Delta H_{\mathrm{dim}}(R_{\mathrm{CC}})$ and $\Delta H^{\mathrm{eq}}_{\mathrm{mon}}$ are heats of formation of dimer at the current intermolecular distance R_{CC} and of monomer in equilibrium, respectively. This energy is evidently complex by nature since, at least, two components contribute into its value, namely, the energy of both monomers deformation $E^{\mathrm{tot}}_{\mathrm{def}}$ and the energy of the covalent coupling $E^{\mathrm{tot}}_{\mathrm{cov}}$ between the monomers. The former component can be determined as

$$E^{\mathrm{tot}}_{\mathrm{def}}(R_{\mathrm{CC}}) = \Delta H^{\mathrm{op}}_{\mathrm{mon1}}(R_{\mathrm{CC}}) + \Delta H^{\mathrm{op}}_{\mathrm{mon2}}(R_{\mathrm{CC}}) - 2\Delta H^{\mathrm{eq}}_{\mathrm{mon}}. \quad (5.2)$$

Here, $\Delta H^{\mathrm{op}}_{\mathrm{mon1}}(R_{\mathrm{CC}})$ and $\Delta H^{\mathrm{op}}_{\mathrm{mon2}}(R_{\mathrm{CC}})$ present the one-point-geometry heats of formation of the skeletons of both monomer molecules of the $C_{60} + C_{60}$ dyad at a given intermolecular distance R_{CC}. The second component $E^{\mathrm{tot}}_{\mathrm{cov}}$ is determined as

$$E^{\mathrm{tot}}_{\mathrm{cov}}(R_{\mathrm{CC}}) = E^{\mathrm{tot}}_{\mathrm{cpl}}(R_{\mathrm{CC}}) - E^{\mathrm{tot}}_{\mathrm{def}}(R_{\mathrm{CC}}). \quad (5.3)$$

The discussed distance-dependent energies are shown in Fig. 5.4. As seen in the figure, the deformation energy is the largest in equilibrium dimer and then steadily decreases when $R_{\rm CC}$ grows, once positive, until approaching zero when monomers are spaced by more than 3 Å. Similarly, the energy of the covalent coupling is the largest in equilibrium dimer then steadily decreases by the absolute value being negative and showing a clearly vivid maximum that coincides with that of $E_{\rm cpl}^{\rm tot}(R_{\rm CC})$. Proceeding with further spacing, the energy falls by the absolute value, changes sign in the vicinity of R^{00} ~4.4 Å, once being small by the absolute value, and then approaches zero for largely spaced monomers. Referring to schemes of electronic terms in Fig. 5.1, one should accept that this is the energy $E_{\rm cov}^{\rm tot}$ that should be attributed to the *netto* barrier profile. However, the energy $E_{\rm cpl}^{\rm tot}(R_{\rm CC})$ as a *brutto* barrier profile will obviously govern the formation of fullerene dimers in practice. Obviously, the obtained barrier is identical to the dimerization barrier that corresponds to the energy-distance dependence when going from initially large spacing between the monomers regularly contracting the latter.

5.3.3 C_{60} Oligomers

The detailed study of the IMI term's profiles, which governs C_{60} dimerization discussed above, opens the way to throw light on peculiarities of the C_{60} oligomerization. Reasonably, the oligomerization can be computationally considered as a stepwise reaction $(C_{60})_n = (C_{60})_{n-1} + C_{60}$ for which the IMI term of the $[(C_{60})_{n-1} + C_{60}]$ dyad controls the formation of the final product $(C_{60})_n$. One cannot exclude more complex scheme, such as $(C_{60})_n = (C_{60})_m + (C_{60})_k$ where $m + k = n$, $(C_{60})_n = (C_{60})_m + (C_{60})_k + (C_{60})_l$ where $m + k + l = n$, and so forth. However, all the schemes are subordinated to common regularities whose main characteristics can be considered for the $(C_{60})_{n-1} + C_{60}$ dyad as an example.

If accepting that the type of IMI terms is mainly determined by $E_{\rm gap} = I_A - \varepsilon_B$ as discussed in Sect. 5.3.1, passing to oligomers one faces a peculiar situation characteristic for fullerenes. The matter is that both ionization potential and electronic affinity of $(C_{60})_n$ oligomer only slightly depend on n and practically coincide with those related to monomer molecule. This can be seen in Table 5.1 for dimer and has been computationally justified for oligomers of complex structure characterized by n varying up to 10 (Sheka et al 2006). Consequently, the IMI term of the $C_{60} + C_{60}$ dyad determines the general behavior of both $(C_{60})_{n-1} + C_{60}$ and $(C_{60})_m + (C_{60})_k$ dyads at each successive step of oligomerization. As in the case of dimers, two products, namely, either $(C_{60})_{n-1} + C_{60}$ or $(C_{60})_m + (C_{60})_k$, charge transfer complexes, and $(C_{60})_n$ oligomer will correspond to equilibrium positions at R^{00} and R^{+-} minima of the IMI term, respectively. Following this suggestion and taking into account the main concepts of computational chemistry of fullerenes, one can suggest a definite scheme of the expected successive oligomerization of C_{60} molecules when going, say, from dimer to tetramer within the $(C_{60})_n = (C_{60})_{n-1} + C_{60}$ oligomerization scheme, as shown in Fig. 5.5.

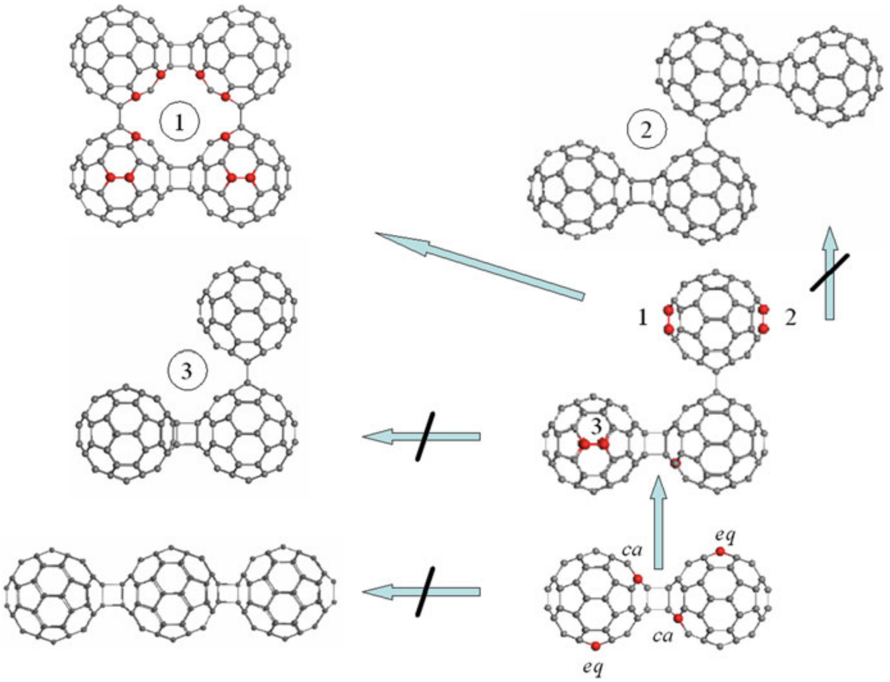

Fig. 5.5 Stepwise oligomerization of C_{60} from dimer to tetramer. Equilibrium structures. *Crossed arrows* indicate unfavorable continuations. Coupling energies constitute –42.23 kcal/mol (dimer); −74.73 kcal/mol (trimer); −164.63 kcal/mol (tetramer 1); −13.84 kcal/mol (tetramer 2); −117.66 kcal/mol (tetramer 3) (Reproduced from Sheka and Shaymardanova (2011b), with permission from the Royal Society of Chemistry)

According to the ACS map of dimer $(C_{60})_2$, there are four pairs of high-rank N_{DA} atoms that are marked by red balls in the right low corner of Fig. 5.5. The first two pairs combine the most reactive atoms adjacent to the cycloaddition (below, contact-adjacent or *ca* atoms) (see atoms 3, 4, 5, and 6 in Fig. 5.3). Next by reactivity four atoms are located in equatorial planes of both monomers (below, equatorial or *eq* atoms). In spite of high chemical reactivity of *ca* atoms, those are not accessible in due course of the further oligomerization so that *eq* atoms of both monomers are actual targets. Following these ACS indication, a right-angle triangle trimer (90°-trimer) must be produced. Therefore, not the "pearl necklace" configuration, intuitively suggested as the most expected for C_{60} oligomerization (Fischer 1994), but more complicated 2D one is favorable for trimerization.

Similarly, the high-rank N_{DA} atoms of trimer as seen in Fig. 5.5 form an incomplete *ca* pair of the highest activity and three pairs of *eq* atoms of comparable activity. Three tetramer compositions, which follow from the high-rank ACS indication related to trimer, are shown in Fig. 5.5. None of them is among the "pearl necklace" family thus presenting 2D tetramers 1 and 2 and 3D tetramer 3.

Among the latter, tetramer 1 possesses the least energy and is expected to continue the oligomerization offering its high-rank N_{DA} atoms, marked by red balls, as targets for the next C_{60} addition. Those form six pairs of the most active *ca* atoms and four pairs of *eq* atoms, position of which dictates the continuation of oligomerization as the formation of 3D configurations of pentamers.

Before passing to comparison with experimental data, it should be noted that the considered oligomerization is related to the addition reaction that occurs between partners in a vacuum without any constrains on their orientation. Empirical reality turns out to be much more complicated since the performed experiments differ quite drastically when going from the study of C_{60} clusters in the gas phase (see Hedén et al. 2005; Enders et al. 2006 and references therein) to that one in solutions (Sun et al. 1995), solid films and powders (Ecklund et al. 1995; Pusztai et al. 1999; Nakayama et al. 1999; Kunitake et al. 2002; Nakaya et al. 2008), and solids (Núñez-Regueiro et al. 1995; Soldatov et al. 2001; Zhang et al. 2010). All the studies clearly evidence the formation of $(C_{60})_n$ clusters with $n = 2$, 3, 4, and more while the information concerning the cluster's structure is rather scarce. The best situation concerns dimers whose dumbbell-like structure was proven by many ways (see Sheka 2007a and references therein). Applying to trimers, there are two sources of information related to different ways of their production that conditionally can be denoted as "chemical" (Kunitake et al. 2002) and "physical" (Nakayama et al. 1999; Nakaya et al. 2008). "Chemical" experiments deal with C_{180} species produced in due course of solid-state mechanochemical reaction under high-speed vibration milling conditions. The final product exhibits two fractions (A and B in the ratio of ~5:4), the former predominantly (~60 %) consisting of 90°-trimers while 100 % of the latter is presented by cyclic 60-trimers. "Physical" experiments deal with trimers produced under photoillumination of either C_{60} films preliminarily deposited on some substrates (Ecklund et al. 1995; Nakayama et al. 1999; Nakaya et al. 2008) or pristine C_{60} crystal (Núñez-Regueiro et al. 1995). Linear three-ball chains were observed in these studies only.

Evidently, all the above experimental procedures put additional restriction on the space where the reactions occur. Here, we are facing a quite unique situation, once a consequence of the simultaneous action of two topologies, one of which is inherent to fullerene molecule while the other is provided by external conditions. From this viewpoint, even a predominant presence of 90°-trimers within fraction A of the "chemical" experiment cannot be considered as a doubtless proof of compositions predicted by the ACS-guided covalent chemistry of C_{60} since three other 108°-, 120°-, and 144°-trimers, observed within fraction A, as well as 60°-trimers of fraction B (Kunitake et al. 2002) seriously contradict the scheme shown in Fig. 5.5. Even more stronger contradiction is revealed by comparison with the "physical" experiments that exhibit only linear "pearl necklace" trimers, the less probable in accordance with the ACS-based analysis. At the same time, compositionally simple "physical" findings evidently connect the trimerization events with a predetermined molecular packing. As known, the latter is evidently the main factor for any topochemical reaction, firstly attributed to fullerenes when explaining both the linear trimerization and linear polymerization of C_{70} in solid state (Soldatov et al. 2001).

From this viewpoint, the production of linear orthorhombic crystalline modification of polymerized C_{60} (Núñez-Regueiro et al. 1995) should be considered as a result of the relevant topochemical reaction. On the other hand, the mechanochemical reaction, responsible for triangle trimers, evidently has a topological odor as well thus providing formation of differently configured trimers due to obvious anisotropy of the stress application to the pristine C_{60} crystal under milling.

The situation with tetramers is not simple, as well. The first suggestion concerning a closed structure of $(C_{60})_4$ clusters analogous to tetramer 1 in Fig. 5.5 was issued for clusters in solutions (Sun et al. 1995). Later on, the suggestion was supported by the analysis of Raman spectra of photoilluminated C_{60} powders (Pusztai et al. 1999) as well as direct STM observation of deposited $(C_{60})_n$ clusters on the (111) surface of gold (Zhang et al. 2010). In spite of a seemingly favorable fitting of the experimental data to the predicted ones, one has to take into account that both experiments are performed under evident conditions that favor topochemical reactions. Thus, not only $(C_{60})_4$ clusters deposited on the gold surface have 2D tetragonal shape similar to tetramer 1 but all other $(C_{60})_n$ clusters with $n > 4$ clearly exhibit 2D configurations in contrast to the predicted 3D ones for pentamers and higher oligomers, which follows from the high-rank N_{DA} ACS indication concerning the tetramer 1 structure shown in Fig. 5.5. The tendency of $(C_{60})_n$ clusters to be inclined to topochemical reaction is uppermost realized in 1D orthorhombic as well as in 2D tetragonal and rhombohedral configurations of polymerized C_{60} crystals, whose production is controlled by varying one-direction contraction of the pristine C_{60} crystal structure at high pressures and temperatures (Núñez-Regueiro et al. 1995).

5.4 Fullerene C_{60} + Carbon Nanotube Composites

5.4.1 Barrier Profile for C_{60}-CNT Nanobuds

There have been known a few attempts to synthesize C_{60} + CNT complexes that present a single structure in which the fullerenes are covalently bonded to the tube body. A few techniques have been suggested to obtain C_{60} + CNT composites in which fullerene is located either inside (see Giacalone and Martín 2010 and references therein) or outside (Li et al. 2003, 2007; Nasibulin et al. 2007a, b) the CNT wall. The terms *peapod* (Giacalone and Martín 2010) and *carbon nanobud* (CNB) (Nasibulin et al. 2007a) were suggested to distinguish the two configurations. For the first time, the C_{60} nanobud based on a single-wall CNT (SWCNT) was obtained by means of solid-phase mechanochemical reactions (Lee et al. 2000). The next time, the C_{60} + SWCNT nanobud was synthesized via a microwave-induced functionalization approach (Li et al. 2003). The findings have led the foundation for a further large investigation aimed at producing fullerene-functionalized SWNTs (Li et al. 2007; Nasibulin et al. 2007b; Tian et al. 2008).

Computational consideration of CNBs has been restricted so far to three publications (Li et al. 2007; Wu and Zeng 2008; Sheka and Shaymardanova 2011b). Two former computations were performed in the framework of the density functional theory (DFT) using periodic boundary conditions (PBCs) in the restricted closed-shell approximation. A few different compositions of intermolecular C–C bonds forming the contact zone on the sidewall of the tubes have been considered among which [2 + 2] cycloaddition turned out to be the most efficient. An alternative approach, which considers the formation of CNB in terms of molecular theory as a result of a DA reaction whose general energetic scheme is presented in Fig. 5.1, is given in the third publication. Broken symmetry approach, based on unrestricted open-shell Hartree-Fock approximation, forms the computations ground. The approach is more suitable for partially radicalized both fullerene C_{60} and CNTs (Sheka and Chernozatonskii 2010b; Sheka 2011a) than above-mentioned restricted DFT one and suggests much more picturesque vision of the CNBs formation and properties.

5.4.2 UBS HF Computational Synthesis of Carbon Nanobuds

Partial radicalization of CNTs is due to a rather strong correlation of their odd electrons (Sheka 2012). The appearance of effectively unpaired electrons is resulted from the exceeding of C–C bond lengths the critical value $R_{\mathrm{cov}}^{\mathrm{crit}}$ (Sheka and Chernozatonskii 2010b), similarly to the situation with fullerenes discussed in Sect. 5.3.1. Distributed over the tube atoms by fractional number of N_{DA}, the effectively unpaired electrons highlight the map of the tube chemical activity in terms of atomic chemical susceptibility (ACS) N_{DA}. Figure 5.6 presents the ACS distribution over atoms of two (4, 4) SWCNTs shown in Fig. 5.7. The tubes differ by the end atom termination only.

As seen in Fig. 5.6, there are three zones in the ACS distribution related to the tube caps, sidewalls, and ends, respectively. Accordingly, one can choose three pairs of target atoms on tube 1 (1, 2, and 3), which are shown by red dots on the curve, and two pairs on tube 2 (4 and 5) shown by red bars. As was discussed in Sect. 5.3.1, the most active atoms of fullerene C_{60} form particularly oriented two hexagons, each atom of which is the target that first meets any addend. The two features, related to chemical portraits of CNTs and fullerene molecule, make it possible to construct five starting configurations of possible [C_{60} + (4,4)] CNBs that alongside with equilibrium structures are presented in Fig. 5.8. The starting intermolecular C–C distances were taken 1.7 Å.

Figure 5.9a, b present changing in the ACS maps of both (4, 4) SWCNT and fullerene C_{60} related to CNB 5. As seen in the figure, the attachment of the fullerene molecule to the sidewall of the tube causes only local changing that concerns atoms participating in the formation of the [2 + 2] cycloaddition. The other part of the atomic activity distribution of the tube retains non-perturbed. This finding evidently favors a multiple attachment of fullerenes to the tube sidewall in a superposition

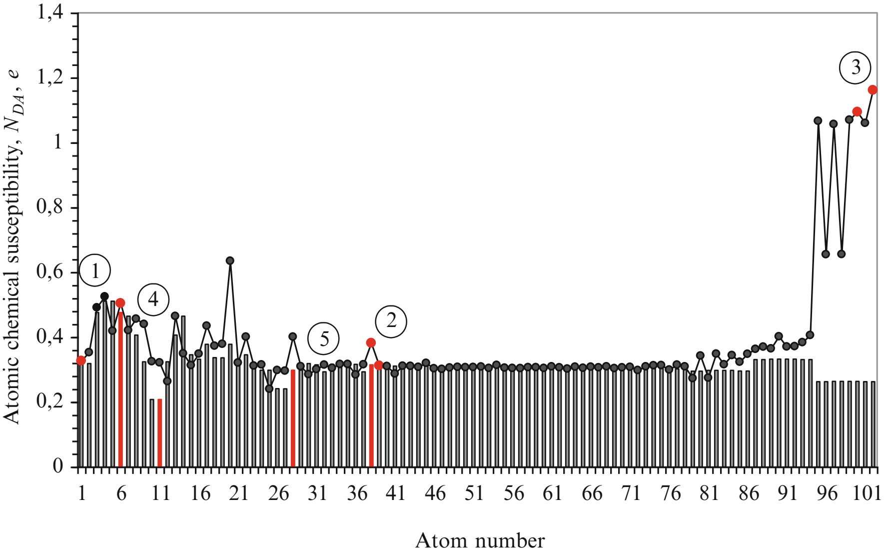

Fig. 5.6 Distribution of the atomic chemical susceptibility N_{DA} over atoms of (4, 4) single-walled carbon nanotubes with empty (*curve* with *dots*) and hydrogen-terminated (histogram) ends (Reproduced with permission from *International Journal of Quantum Chemistry*, Sheka and Chernozatonskii 2010c. Copyright (2010) by John Wiley & Sons, Inc.). The atom numbering corresponds to that one over the tubes from the tube caps to their ends. *Ringed numbers* denote atom pairs subjected to further C_{60} addition (see text)

Fig. 5.7 Equilibrium structures of (4, 4) single-walled carbon nanotube with empty (tube 1) (**a**) and hydrogen-terminated (tube 2) (**b**) ends

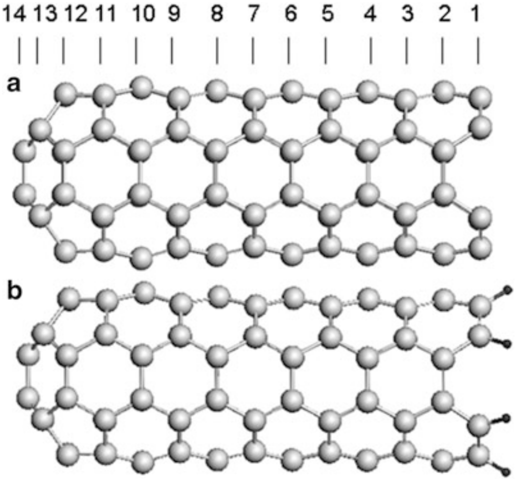

manner. Oppositely, the fullerene ACS map changes considerably indicating a significant redistribution of the atomic chemical activity over the molecule atoms after attachment. Red dots on plotted curve in Fig. 5.9b highlight new the most active atoms prepared for the next reaction events.

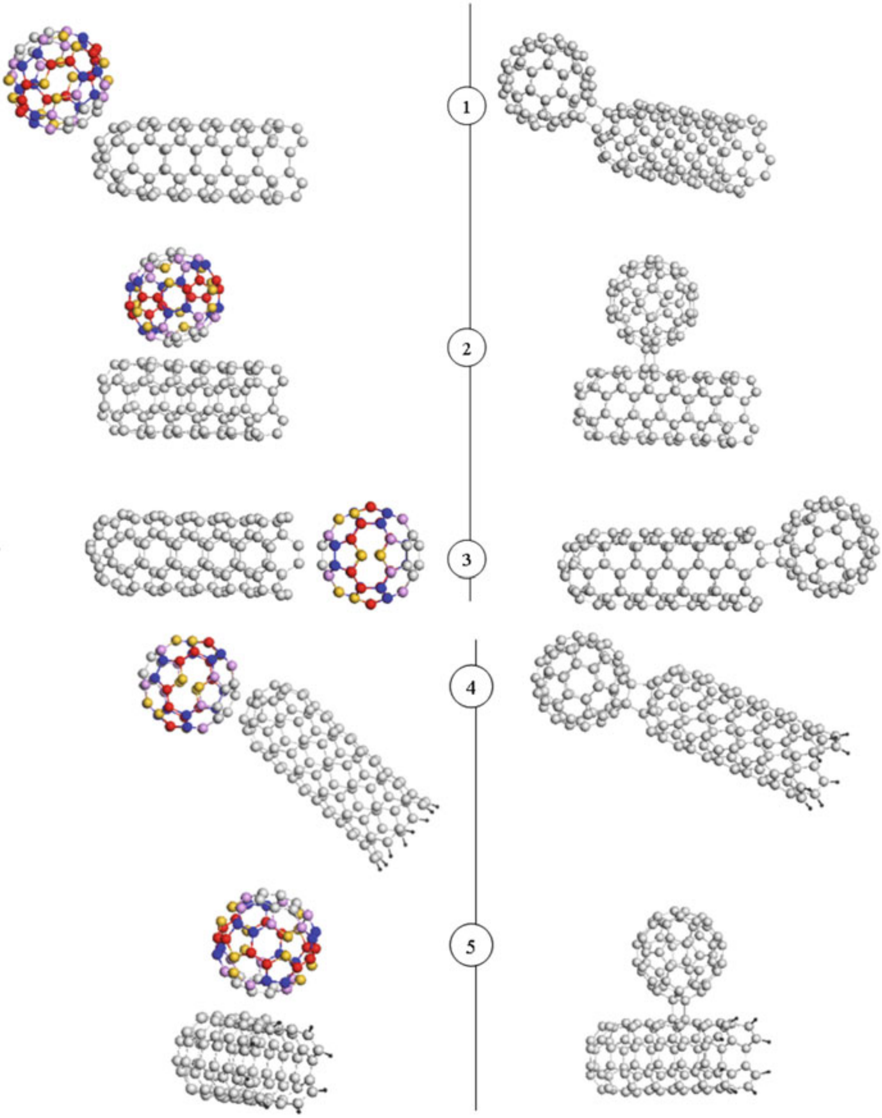

Fig. 5.8 Starting (*left*) and equilibrium (*right*) structures of carbon nanobuds formed by attaching C_{60} to (4, 4) single-walled carbon nanotube with empty (1–3) and hydrogen-terminated (4, 5) ends. Figures number the nanobuds (Reproduced from Sheka and Shaymardanova 2011b, with permission from the Royal Society of Chemistry)

To check a high tolerance of the tube body to a multiple attachment of the fullerene molecules, two and three C_{60} molecules were attached to an elongated (4, 4) SWCNT (tube 3) forming CNB 6 and CNB 7 (see Fig. 5.10). As shown (Sheka and Chernozatonskii 2010b), the tube elongation causes the elongation of

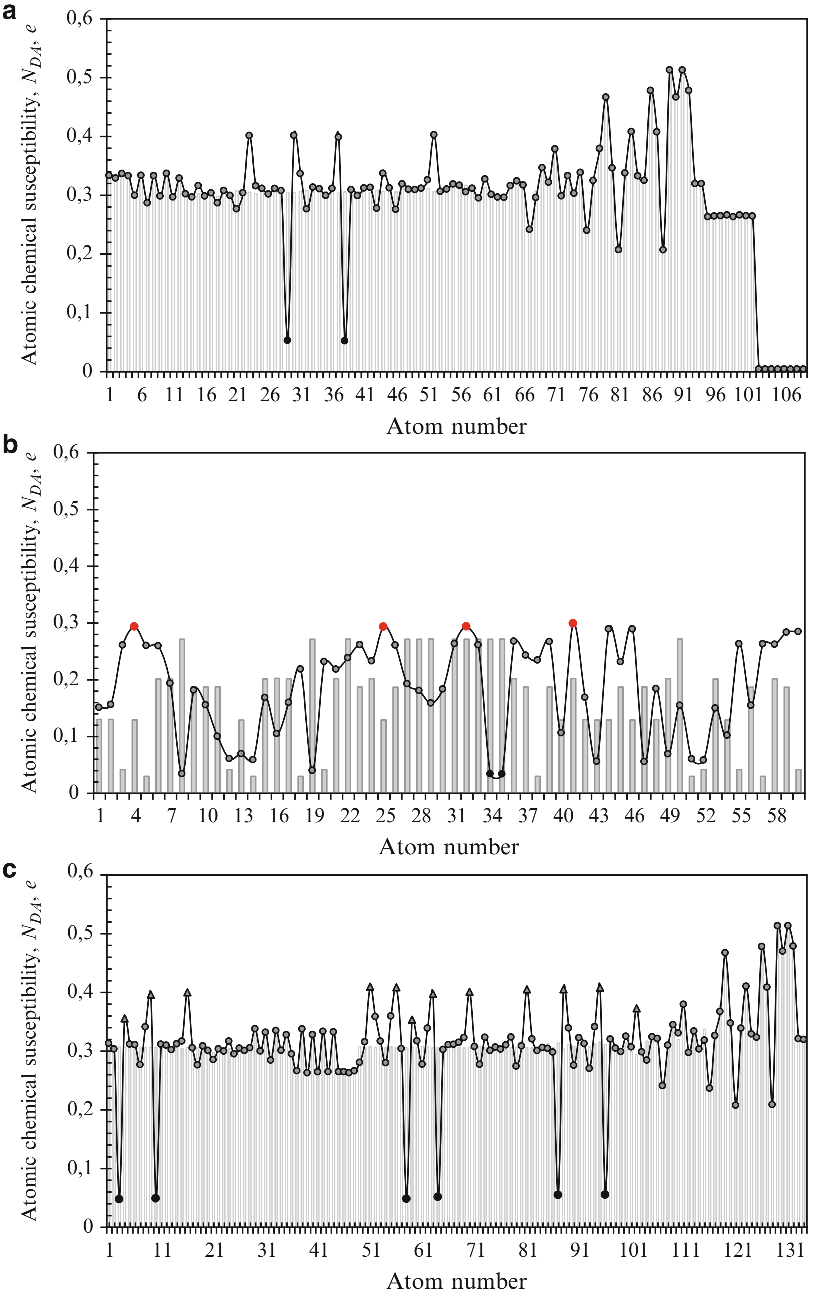

Fig. 5.9 Evolution of the atomic chemical susceptibility distribution caused by carbon nanobuds formation. (**a**) Tube 2 (CNB 5); (**b**) fullerene C_{60} (CNB 5); (**c**). tube 3 (CNB 7) (see text). Histograms present data for the pristine species (Reproduced from Sheka and Shaymardanova 2011b, with permission from the Royal Society of Chemistry). *Curve* with *dots* plot data related to the formed CNBs

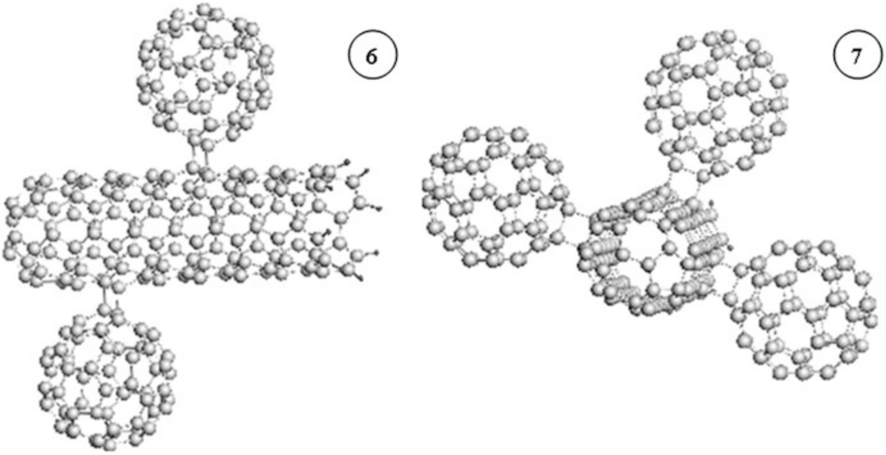

Fig. 5.10 Equilibrium structures of [C_{60} + (4, 4)] CNBs related to double (CNB 6) and triple (CNB 7) attachments of C_{60} to the sidewall of (4, 4) single-walled carbon nanotube with hydrogen-terminated ends (Reproduced from Sheka and Shaymardanova (2011b), with permission from the Royal Society of Chemistry)

the sidewall zone in the ACS map only and does not touch either cap or end atom regions. That is why the conditions for the formation of CNBs 5, 6, and 7 are practically identical. All the attached C_{60} molecules are joined with the tube sidewall via [2 + 2] cycloadditions. Changing in the ACS distribution related to tube 3 is shown in Fig. 5.9c. A clearly seen superposition of the three attachments is perfectly exhibited by the map, indicating that practically countless number of fullerene molecules can be attached to SWCNTs long enough.

Figure 5.11 presents a collection of typical [C_{60} + (4,4)] CNBs whose detail analysis shows that the intermolecular junctions as [2 + 2] cycloadditions are formed only in the case when fullerene is covalently coupled with the tube sidewalls. This concerns CNBs 2, 6, and 7 while the junctions in CNBs 1 and 3 are not [2 + 2] cycloaddition in spite of four-atom membership. Coloring most active fullerene atoms highlights targets on the C_{60} body that may stimulate a further chemical modification of the CNBs. As seen in the figure, in all the cases of [2 + 2] cycloadducts, the evolution of chemical activity of fullerene in CNBs is the same and practically identical to that one typical for the C_{60} oligomerization (ca. Fig. 5.5). As previously, the most active atoms form pairs of contact-adjacent *ca* atoms that are followed by slightly less active equatorial *eq* atoms. Obviously, *ca* atoms are accessible only for small addends while *eq* atoms take the responsibility on themselves when continuing the CNBs chemical modification via subsequent expanded attachments to the fullerene that intend to be the best suitable for a particular application. As for CNBs 1 and 3, the situation is somewhat different. However, a predetermined position of *ca* and *eq* atoms makes a further modification of CNBs via attached C_{60} predictable and controlled in all the cases.

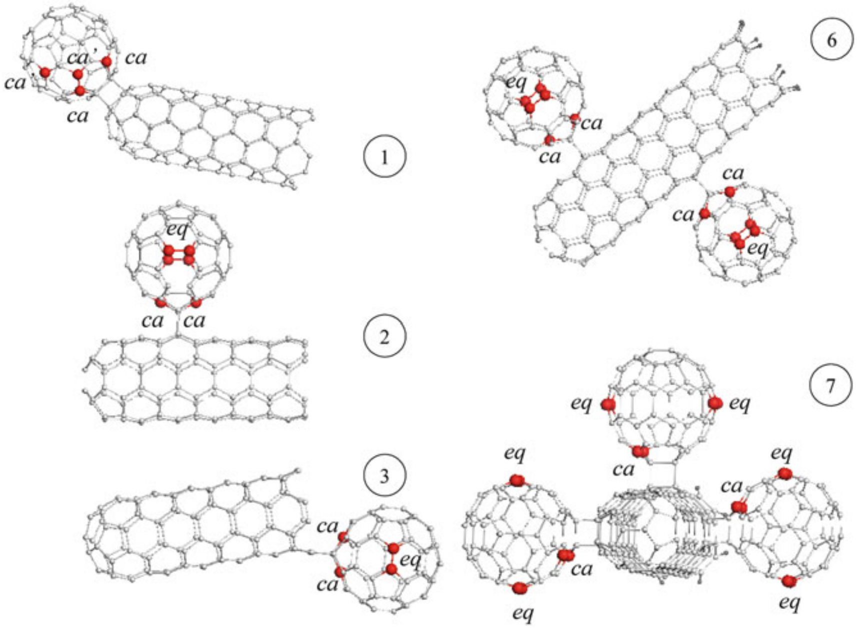

Fig. 5.11 Equilibrium structures of [C_{60} + (4, 4)] CNBs (Reproduced from Sheka and Shaymardanova (2011b), with permission from the Royal Society of Chemistry). *Red balls* indicate atoms of fullerene C_{60} with the high-rank N_{DA} values

Table 5.2 Energetic characteristics of equilibrium [C_{60} + (4,4)] CNT nanobuds, kcal/mol

Nanobuds[a]	E_{cpl}^{tot}	E_{def}^{tot}	$E_{def\,CNT}$	$E_{def\,C_{60}}$	E_{cov}^{tot}
1. (cap)	−36,33	51,16	10,62	40,53	−87,48
2. (wall)	−3,38	59,64	24,64	35	−63,02
3. (end)	−86,65	47,65	8,25	39,4	−134,31
4. (cap)	3,09	114,38	62,76	51,62	−111,29
5. (wall)	−4,26	74,33	39,26	35,07	−78,59
6. (wall)	−8,21 (−4,10)[b]	155,62	85,33 (42,66)[b]	70,29 (35,15)[b]	−163,83 (−81,92)[b]
7. (wall)	−11,02 (−3,67)[b]	221,64	116,59 (38,86)[b]	105,05 (35,02)[b]	−232,66 (−79,55)[b]

Reproduced from Sheka and Shaymardanova (2011b), with permission from the Royal Society of Chemistry

[a] Figures number CNBs as in Figs. 5.8 and 5.10

[b] Data per one attached C_{60} molecule

5.4.3 Energetic Parameters and Reaction Barrier of Carbon Nanobuds

Energetic characteristics related to a set of [C_{60} + (4,4)] CNBs are presented in Table 5.2. The coupling energy E_{cpl}^{tot} is determined as

$$E_{cpl}^{tot} = \Delta H_{CNB} - \Delta H_{CNT} - \Delta H_{C_{60}}. \quad (5.4)$$

Here, ΔH_{CNB}, ΔH_{CNT}, and $\Delta H_{\mathrm{C}_{60}}$ present heats of formation of the equilibrium structures of CNB, (4,4) SWCNT, and C_{60}, respectively.

As discussed in Sect. 5.3.2, the total coupling energy reflects two processes that accompany the fullerene attachment to the tube, namely, the deformation of both CNB components and their covalent coupling. The energy caused by deformation is determined as

$$E_{\mathrm{def}}^{\mathrm{tot}} = E_{\mathrm{def\,CNT}} + E_{\mathrm{def\,C}_{60}}, \tag{5.5}$$

where

$$E_{\mathrm{def\,CNT}} = \Delta H_{\mathrm{CNT/CNB}}^{\mathrm{op}}(R_{\mathrm{CC}}) - \Delta H_{\mathrm{CNT}}^{\mathrm{eq}} \text{ and } E_{\mathrm{def\,C}_{60}} = \Delta H_{\mathrm{C}_{60}/\mathrm{CNB}}^{\mathrm{op}}(R_{\mathrm{CC}}) - \Delta H_{\mathrm{C}_{60}}^{\mathrm{eq}}. \tag{5.6}$$

Here, $\Delta H_{\mathrm{CNT/CNB}}^{\mathrm{op}}(R_{\mathrm{CC}})$ and $\Delta H_{\mathrm{C}_{60}/\mathrm{CNB}}^{\mathrm{op}}(R_{\mathrm{CC}})$ present heats of formation of the one-point-geometry configurations of the SWCNT and fullerene components of the CNBs equilibrium configurations corresponding to the intermolecular distance R_{CC}. Accordingly, the chemical contribution into the coupling energy is determined as

$$E_{\mathrm{cov}}^{\mathrm{tot}} = E_{\mathrm{cpl}}^{\mathrm{tot}} - E_{\mathrm{def}}^{\mathrm{tot}}. \tag{5.7}$$

The data listed in Table 5.2 show two distinct features. The first concerns the difference in the energetic characteristics of CNBs, fullerene component of which is attached to either the cap or end atoms of the tube. The second is related to a close similarity of the latter for CNBs with fullerene attached to the tube sidewall. As seen in the table, the empty end of the tube, once the most active according to the ACS map in Fig. 5.6, provides the fullerene attachment with the biggest coupling energy and the smallest deformation energy related to the tube. It means that, at any contact of such tube with fullerene (as well as with any other addend), the first attachment occurs at the tube end. The next events will take place at the tube cap. The coupling energy decreases by 2.4 times while the deformation energy slightly increases. After these two events, there comes a turn of the tube sidewall, but the coupling energy decreases by ~26 times when the deformation energy increases three times. The three events are quite superpositional as can be seen in Fig. 5.12. Each addition concerns a strictly local area so that highly active attachments to the end and cap region should not prevent from covering the main tube body by multiple attached fullerenes.

Figure 5.13 presents the dependence of the basic energetic characteristics of the CNBs on the C–C intermolecular distance R_{CC} by the example of CNB 5. As in the case of fullerene dimers discussed in Sect. 5.3.2, the barrier energy computation follows a stepwise elongation of two C–C bonds, which provide intermolecular contact via $[2+2]$ cycloaddition, starting from the equilibrium configuration of the bud. The first minimum of the coupling energy $E_{\mathrm{cpl}}^{\mathrm{tot}}$ is located at $R_{\mathrm{CC}} = 1.57$ Å and constitutes −4.26 kcal/mol. The maximum position at 2.05 Å shows that at starting

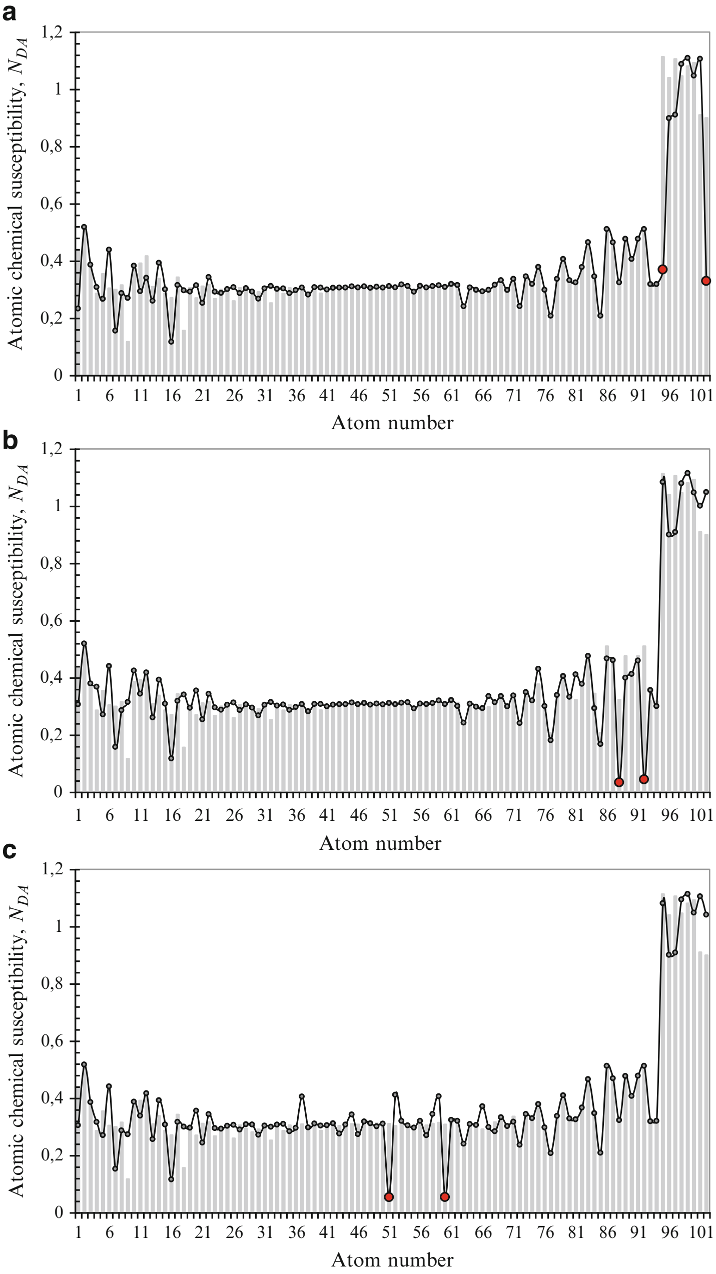

Fig. 5.12 Evolution of the atomic chemical susceptibility distribution over tube 1 under CNB formation when C_{60} is attached to the tube empty end (**a**), cap (**b**), and sidewall (**c**) (Reproduced from Sheka and Shaymardanova (2011b), with permission from the Royal Society of Chemistry). Histograms present data for the pristine tube. *Curves* with *dots* plot the data related to the formed CNBs 1, 2, and 3, respectively. *Circled dots* mark atoms, to which fullerene is attached. Atom numbering corresponds to that one in the output files

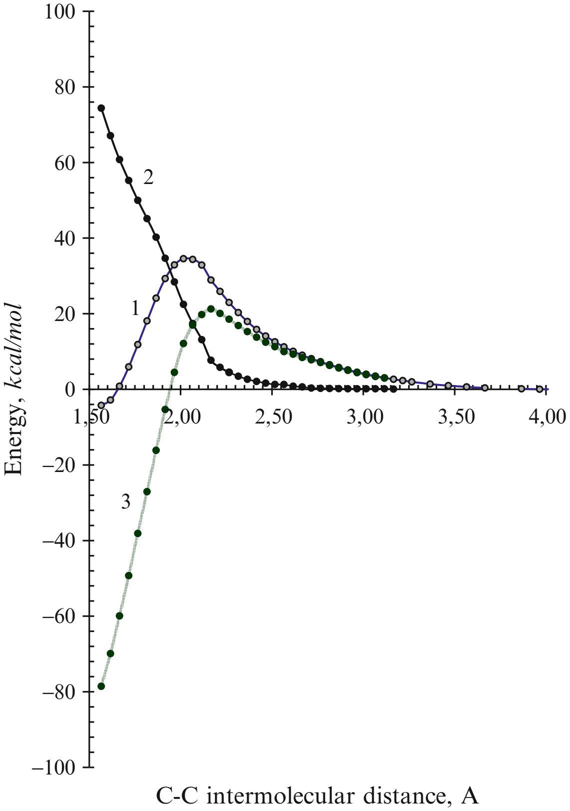

Fig. 5.13 Profile of the barrier of the [C_{60} + (4, 4)] CNB decomposition (CNB 5) (Reproduced from Sheka and Shaymardanova (2011b), with permission from the Royal Society of Chemistry). *1.* $E^{\text{tot}}_{\text{cpl}}(R_{\text{CC}})$; *2.* $E^{\text{tot}}_{\text{def}}(R_{\text{CC}})$; *3.* $E^{\text{tot}}_{\text{chem}}(R_{\text{CC}})$ (see text)

distances exceeding this value, CNT and C_{60} form a weakly coupled complex with equilibrium spacing between components of 4.47 Å and coupling energy of −0.06 kcal/mol. The complex possesses all the characteristics of the charge transfer one, where CNT donates while C_{60} accepts electron under photoexcitation. Here we meet again the confirmation of the "4.2–4.7 Å" rule that governs photodimerization and/or oligomerization of C_{60} molecules discussed in Sect. 5.3.1. A deep parallelism in the behavior of fullerene molecules, either singly bound to the tube body or in a company with other molecules in the case of multiple attachments, provides a good reason to expect the same parallelism between the energy dependences for these molecules, as well.

Since the contact zone between components of $(C_{60})_2$ dimer and the considered CNB is presented by [2 + 2] cycloaddition, one could expect a deep similarity in the barrier profiles in the two cases. However, a comparison of plottings presented in Figs. 5.4 and 5.13 has revealed that this expectation has been realized only partially. Actually, one can see a similarity of the profile shape related to both the total coupling energy $E^{\text{tot}}_{\text{cpl}}$ and $E^{\text{tot}}_{\text{def}}$, $E^{\text{tot}}_{\text{cov}}$ components in both cases. At the same time, the difference in numerical values of all the energies is so pronounced that starting at much shallower minimum of $E_{\mathrm{cpl}}^{\mathrm{tot}}$ in the case of CNB, much lesser barrier for the CNB formation and/or decomposition is achieved. So far no explanation of the difference other than the revealing of topochemistry of the addition reactions $C_{60} + C_{60}$ and C_{60} + CNT can be suggested. A deep analysis of similar reactions for C_{60} + NGr dyads, given in the next section, convincingly supports the suggestion and exempts it from the last doubts.

5.5 Fullerene C_{60} + Graphene Composites

5.5.1 Barrier Profile for C_{60} + NGr Nanobuds

In contrast to fullerene oligomers and carbon nanobuds, the latter known now not only for C_{60} but for C_{70} as well (Nasibulin et al. 2007b; Tian et al. 2008), no indication of the existence of chemically bound fullerene-NGr compositions has been so far obtained. In contrast, it is worthwhile to remind a curious observation of intercalation of a graphite monolayer (authors' term) on iridium substrate by C_{60} molecules from a thick film made of fullerene deposited over graphene at $T \sim 800$ K (Rut'kov et al. 1995), which speaks about a quite particular binding of the fullerene molecule with graphene.

Computations performed by Wu and Zeng (2009) were first to lift the veil above the feature. They have shown that the reaction of covalent addition of C_{60} to graphene basal plane is endothermic and requires a considerable amount of energy in contrast to $(C_{60})_2$ dimer and [C_{60} + (4,4)] CNBs discussed in Sects. 5.3 and 5.4. However, the mentioned computations have been carried out in a standard configuration of the spin-restricted close-shell PBC DFT approach in spite of the fact pointed by the authors themselves that local and semilocal functionals in DFT generally give poor description of weak interaction. Similarly, insufficient is the response of the technique to the correlated odd electrons of graphene that is why test calculations of the authors within a spin-unrestricted DFT could not show any difference from the spin-restricted one due to overpressing the configurational part of the functionals. Similar test performed within the framework of the UBS HF approach (Sheka and Shaymardanova 2011b) results in 23 % (or 641.6 kcal/mol by the absolute value) lowering of the total energy of the (9, 9) NGr (the nomenclature follows the suggested in Gao et al. (2008)), which was chosen as supercell in the PCB DFT computations (Wu and Zeng 2009), when going from RHF to UBS HF approach.

Besides what has been said above, describing possibility to arrange periodic graphene nanobuds (GNBs), Wu and Zeng concentrated their attention on the basal plane of (9, 9) NGr as a substrate for a single C_{60} leaving the sheet edges aside as well as supposing homogeneous chemical activity of carbon atoms through over the sheet. It is actually not the case since a high non-homogeneity in the ACS distribution over NGr atoms divides its space into three regions, namely, zigzag and armchair edges and the basal plane (Sheka and Chernozatonskii 2010c, d) similarly to cap, end, and sidewall of SWNT discussed in the previous section. This circumstance forms the grounds for the dependence of the formed nanobuds from the place of location of C_{60} and the state-of-the-art termination of both end and edge atoms. Empirically, the extreme chemical activity of the graphene edge atoms has been observed for various addends (Yan et al. 2012). Computationally, it has been predicted for such addends as carbon nanotubes (Sheka and Chernozatonskii 2010a) and C_{60} (Sheka and Shaymardanova 2011a). Obviously, the feature is of a particular importance for elaborating technology of producing graphene-based nanocarbon composites.

As was shown by the example of fullerene C_{60} (Sheka 2011a), the best way to eliminate features related to spatial inhomogeneity of the chemical activity of the molecule is to perform a computational stepwise synthesis of the derivatives in an algorithmic manner following the high-rank ACS value at each addition step. However, when the molecule is spatially extended such as CNTs and graphene sheets, different parts of the molecules may enter the reaction simultaneously, which drastically complicates the computational analysis, particularly when these parts are characterized by different chemical activity as is the case of CNT and graphene and when their electronic systems are interconnected. This circumstance faces one the problem of the substitution of a single-reaction approach usually used at simulations with a multi-reaction one. So far there has not been any multiple-reaction approach that could consider a simultaneously occurring community of reactions under so complicated conditions. A conventional single-reaction approach, applied to either solitary or stepwise reaction, can describe a multiple reaction only if the latter presents a set of events, nondependent on each other. As shown in the preceding section, such an approach was quite accessible for the description of CNBs. A similar superpositional approach was applied in Sheka and Shaymardanova (2011b) to the $[C_{60} + (5, 5)]$ GNB to trace the dependence of the reaction product on the place of contact of the C_{60} molecule with (5, 5) NGr. As previously with dimer $(C_{60})_2$ and CNBs, each of the reaction related to the formation of $[C_{60} + (5, 5)]$ GNB is considered in terms of the scheme shown in Fig. 5.1.

5.5.2 Computational Single-Reaction Synthesis of Graphene Nanobuds

Similarly to fullerenes and CNTs, the length of C–C bonds in graphene noticeably exceeds the critical value $R_{\text{cov}}^{\text{crit}}$ at which a complete covalent bonding of the relevant odd electrons is terminated, so that odd electrons of graphene are quite strongly correlated (Sheka 2011a, 2012) and effectively unpaired, thus providing quite valuable molecular chemical susceptibility N_{D} of the NGr molecule as a whole and noticeable atomic chemical susceptibility (ACS) N_{DA} related to each atom. Distributed over the NGr atoms, N_{DA} maps the chemical activity of the molecule atoms. Figure 5.14 presents the ACS distributions over atoms of (5, 5) NGr under

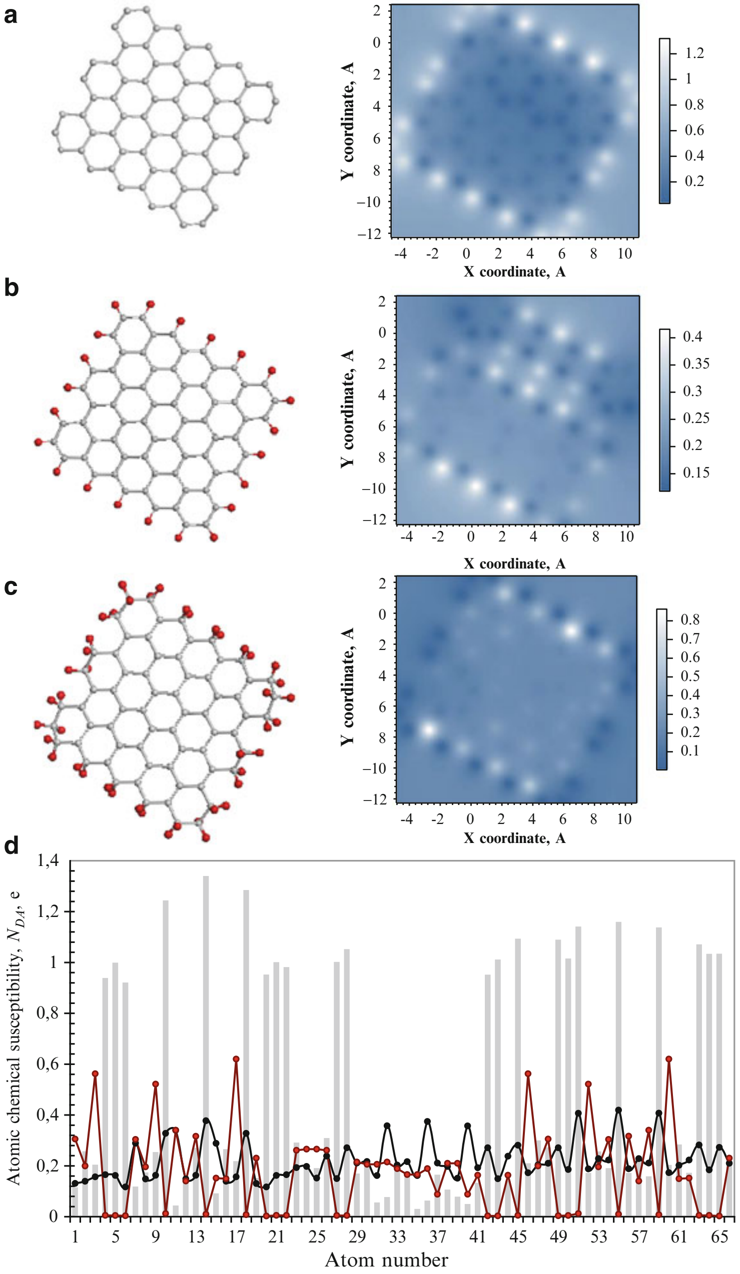

Fig. 5.14 Equilibrium structures (*left*) and chemical portraits (*right*) of (5, 5) nanographene with empty (**a**) and hydrogen-terminated edge atoms by one (**b**) and two (**c**) terminators per carbon atom. Vertical scales determine the N_{DA} values amplitude. Distribution of the chemical susceptibility over nanographene atoms (**d**) *light gray* histogram (*a*), *black curve* with *dots* (*b*), and *dark red curve* with *dots* (*c*) (Reproduced from Sheka and Shaymardanova (2011b), with permission from the Royal Society of Chemistry)

conditions when the sheet edges are either non-terminated (empty) (a) or hydrogen-terminated by one (single-H) (b) and two (double-H) (c) atoms per one carbon. The color pictures present "chemical portraits" of the three molecules while plotting in Fig. 5.14d discloses the ACS distributions by the absolute values.

As seen in the figure, the portraits diverge considerably exhibiting the difference in both molecular and atomic chemical activity making the three molecules absolutely different with respect to the same chemical reactions. Non-terminated sheet is the most reactive. Then follow single-H- and double-H-terminated ones, the latter is the least active with respect to the total molecular susceptibility. In the case of C_{60}, its addition to the graphene sheet will obviously occur quite differently depending on particular-edge sample and the place of contact to the latter. Since zigzag and armchair edges as well as basal plane are the main space marks of graphene, let us consider possible situations concerning the C_{60} attachment to the (5, 5) NGr in view of the variation of both contact places and chemical termination of edge atoms. Each place-located reaction will be analyzed basing on the ACS distribution over the atoms related to the chosen place configuration.

As turned out, in all the cases, the chemically bound products are formed when the starting intermolecular C–C distances are less than 2.0 Å. At longer distances, each pair of C_{60} and (5, 5) NGr forms a classical charge transfer complex where graphene's atoms contribute into the HOMO while C_{60}'s atoms govern the LUMO, which causes the charge transfer from NGr to fullerene under photoexcitation.

5.5.2.1 Deposition of C_{60} on (5, 5) Nanographene with Non-terminated Edges

According to the ACS map in Fig. 5.14a, atoms of zigzag empty edges are characterized by the highest ACS values. Approaching the edge, fullerene molecule will orient itself in such a way to provide the closeness between its most reactive atoms with two zigzag carbon atoms thus providing the formation of GNB 1 (see Fig. 5.15). Equilibrium structure of the formed GNB is shown next to the start configuration alongside with the ACS maps related to the graphene constituent of the GNB formed. Energetic parameters are presented in Table 5.3. We shall refer so far to the total coupling energy $E_{\mathrm{cpl}}^{\mathrm{tot}}$ only, leaving the discussion of other quantities to the next section. The coupling energy is determined as

$$E_{\mathrm{cpl}}^{\mathrm{tot}}(R_{\mathrm{CC}}) = \Delta H_{\mathrm{GNB}}(R_{\mathrm{CC}}) - \Delta H_{\mathrm{NGr}}^{\mathrm{eq}} - \Delta H_{\mathrm{C}_{60}}^{\mathrm{eq}}, \tag{5.8}$$

where $\Delta H_{\mathrm{GNB}}(R_{\mathrm{CC}})$, $\Delta H_{\mathrm{NGr}}^{\mathrm{eq}}$, and $\Delta H_{\mathrm{C}_{60}}^{\mathrm{eq}}$ determine heats of formation of the considered equilibrium GNB, characterized by intermolecular distance R_{CC} as well as equilibrated NGr and fullerene C_{60}, respectively. As seen in the table, GNB 1 formation is accompanied by high coupling energy whose negative sign points to the energetically favorable process.

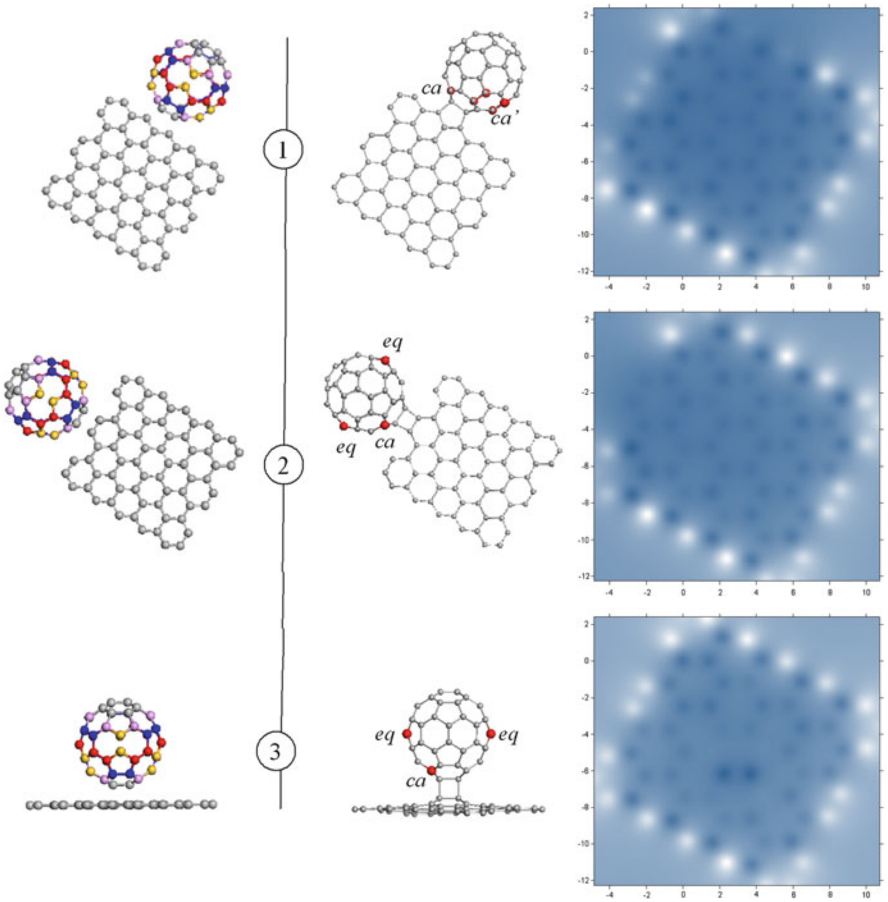

Fig. 5.15 [C_{60} + (5, 5)] graphene nanobuds formed by attaching C_{60} fullerene to zigzag (*1*) and armchair (*2*) edge atoms as well as to the basal plane (*3*) of (5, 5) nanographene. Starting (*left*) and equilibrium (*right*) configurations with ACS maps of the latter. *Red balls* on equilibrium structures point fullerene atoms with the high-rank ACS values (Reproduced from Sheka and Shaymardanova (2011b), with permission from the Royal Society of Chemistry)

Looking at the ACS map of GNB 1 in Fig. 5.15, one can easily trace the effect of C_{60} attachment to the graphene substrate. Thus, two brightly shining zigzag atoms in the left, upper corner of the map in Fig. 5.14a are substituted with two dark spots in Fig. 5.15 while ACS of the remainder atoms is less altered. The quantified change in the ACS is presented by plottings in Fig. 5.16. The behavior of the attached fullerene seems to be quite similar to that considered in the previous sections. The molecule remains still chemically active. Its ACS map considerably changes after addition revealing new target atoms shown by red balls on equilibrium structures. The fullerene activity zone is quite similar to that one related to CNB 1 in Fig. 5.11 that should be expected due to zigzag structure of the (4, 4) SWCNT open end.

Table 5.3 Energetic characteristics of equilibrium [C_{60} + (5,5)] graphene nanobuds, kcal/mol

Composite[a]	$E_{\mathrm{cpl}}^{\mathrm{tot}}$	$E_{\mathrm{def}}^{\mathrm{tot}}$	E_{defgr}	$E_{\mathrm{def}\,C_{60}}$	$E_{\mathrm{chem}}^{\mathrm{tot}}$
1. zg	−128,45	70,56	20,7	49,86	−199,01
2. ach	−123	52,67	13,37	39,3	−175,67
3. bs	−12,11	86,8	53,76	33,04	−98,91
4. zgH1	−52,74	109,89	69,08	40,81	−162,63
5. achH1	−70.17	91.53	58.10	33.44	−161.71
6. bsH1	−27,38	96,63	63,48	33,25	−124,11
7. bsH2	1,82	62,24	28,97	33,27	−60,42
8. bsH1[b]	32	88,98	55,75	33,23	−56,98

Reproduced from Sheka and Shaymardanova (2011b), with permission from the Royal Society of Chemistry

[a] Figures correspond to GNB's numbers in Figs. 5.15, 5.18, and 5.19

[b] Data for [C_{60} + (9, 8)] GNB

Graphene nanobuds 2 and 3 in Fig. 5.15 are formed by attaching fullerene C_{60} to either armchair edge of the graphene sheet or its basal plane. The intermolecular junctions look like characteristic [2 + 2] cycloadditions in both cases. However, a typical [2 + 2] junction, identical to that one for C_{60} oligomers and CNBs, takes place in GNB 3 only. In the case of GNB 2, the four-atom contact zone is supported by carbon atoms with two neighbors from the graphene side while the support atoms of fullerene have three neighbors. In spite of the difference, the junctions provide a high similarity in the construction of the fullerene active zones in the two cases. The latter consists of pairs of contact-adjacent *ac* and equatorial *eq* atoms and is fully identical to those discussed earlier for [2 + 2] cycloadducts related to both C_{60} oligomers and CNBs. Any further chemical modification of the GNBs via fullerene will depend on the addend size and will be favorable by targeting *ca* atoms by small addends while becoming preferable when targeting *eq* atoms by bulky addends. In contrast to structural similarity, energetic parameters of the two GNBs are quite different. If those for GNB 2 are similar by value to those of GNB 1, the coupling energy $E_{\mathrm{cpl}}^{\mathrm{tot}}$ of GNB 3 is more than ten times fewer by the absolute value.

At first glance, the relevant ACS maps in Fig. 5.15 and their plottings in Fig. 5.16 evidence a quite local character of the C_{60} attachment to the graphene sheet. This might allow for suggesting a superpositional multiple attachment of the molecule forming multiple [$(C_{60})_n$ + (5, 5)] GNBs looking like one of numerous possible examples presented in Fig. 5.17a. In its turn, attached fullerenes might serve as centers for further chemical modification of the GBDs by the formation of branched chains of different configurations (see Fig. 5.17b). However, in contrast to the above-considered CNBs, the fullerene attachment to the graphene sheet causes rather noticeable perturbations in the odd electronic state of the graphene, different in the considered three cases, as seen in Fig. 5.16. This feature may indicate a non-locality of the contact zones and puts a serious question concerning a superpositional character of multiple C_{60} attachments similar to those shown in Fig. 5.17a.

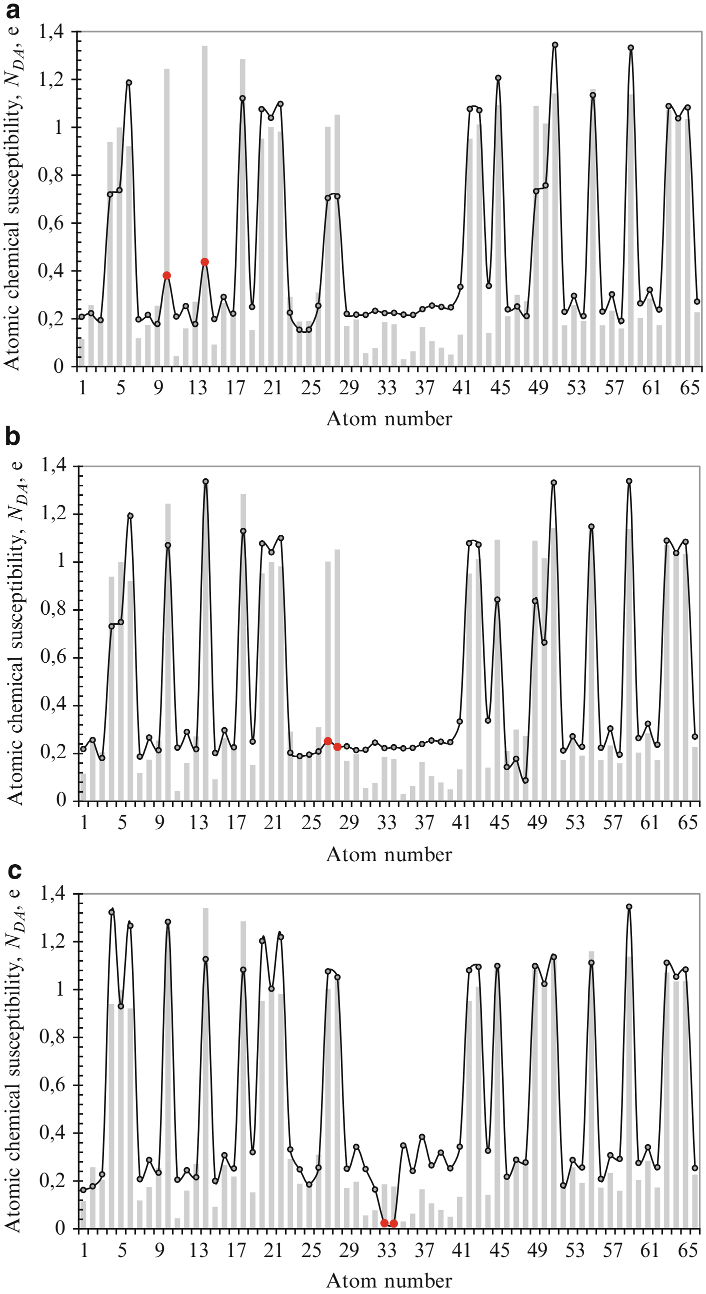

Fig. 5.16 Atomic chemical susceptibility distribution over graphene atoms (*curves* with *dots*) in [C_{60} + (5, 5)] graphene nanobuds: GNB 1 (**a**), GNB 2 (**b**), and GNB 3 (**c**). *Red balls* mark graphene atoms to which C_{60} is covalently attached. *Light gray* histograms present ACS distribution for the pristine empty-edge (5, 5) nanographene (Reproduced from Sheka and Shaymardanova (2011b), with permission from the Royal Society of Chemistry)

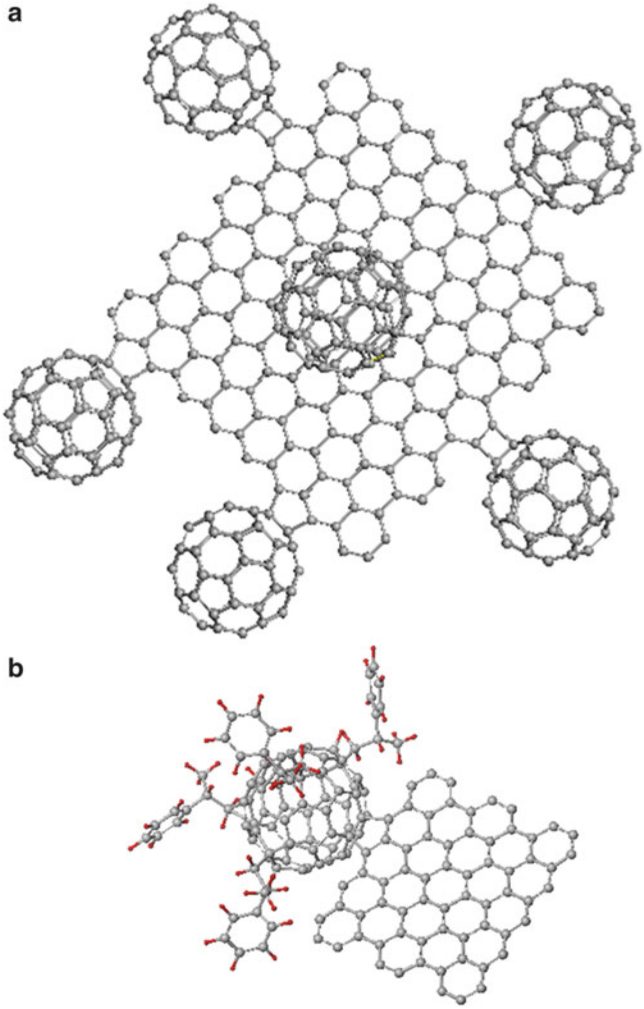

Fig. 5.17 (**a**) A multiple $[(C_{60})_6 + (5{,}5)]$ graphene nanobud. (**b**). $[\{C_{60}Styr_4\} + (5{,}5)]$ graphene nanobud with C_{60}-tetrastyrene

5.5.2.2 Deposition of C_{60} on (5, 5) Nanographene with Hydrogen-Terminated Edges

Figure 5.18 presents single-reaction GNBs that can be formed in this case. As seen in the figure, the $[C_{60} + (5{,}5)]$ GNBs' behavior is similar to that described in the previous section concerning the character of the graphene perturbation, the dependence on the place of contact, and the contact zone configurations. In the case of double-H-terminated graphene, the activity of zigzag and armchair edges is fully suppressed so that only contacts on the basal plane take place in the GNB

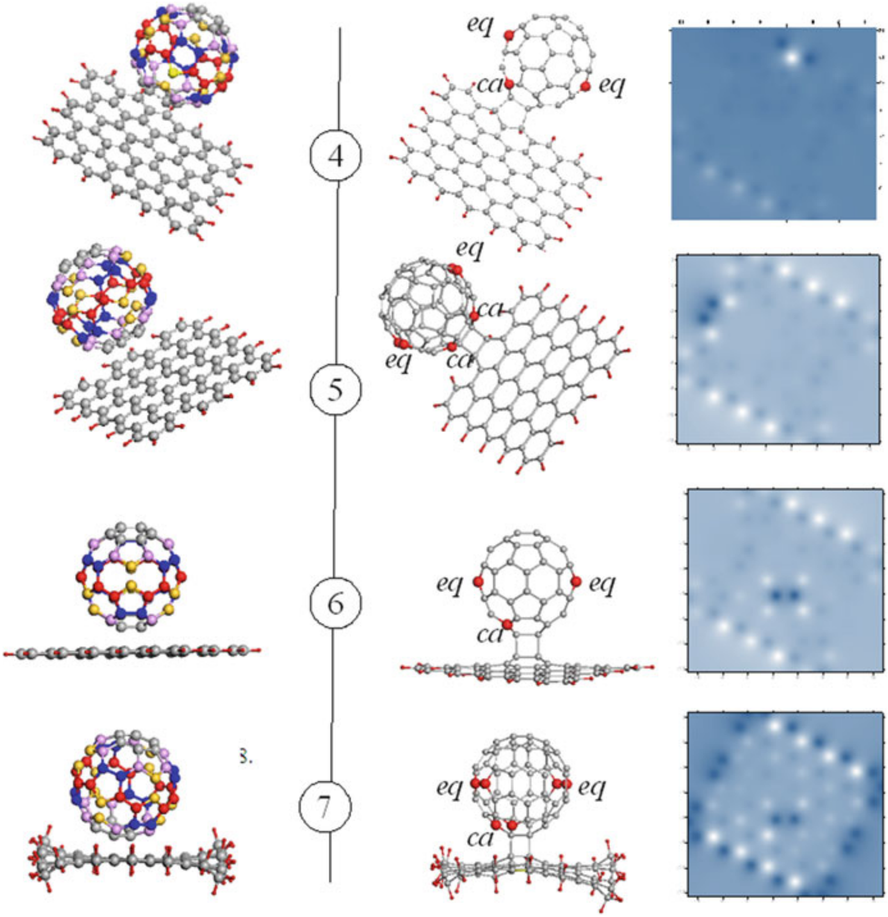

Fig. 5.18 [C_{60} + (5, 5)] graphene nanobuds formed by attaching C_{60} fullerene to zigzag (*4*) and armchair (*5*) edge atoms as well as to the basal plane (*6*) and (*7*) in the case of single-H (4–6)- and double-H (7)-terminated (5, 5) nanographene. Starting (*left*) and equilibrium (*right*) configurations with ACS maps of the latter. *Red balls* on equilibrium structures point to fullerene atoms with the high-rank ACS values (Reproduced from Sheka and Shaymardanova (2011b), with permission from the Royal Society of Chemistry)

formation. As previously, the contact zones of GNBs 4 and 5 are not explicitly [2 + 2] cycloaddition junctions while those of GNBs 6 and 7 belong to the latter.

Changes in the chemical activity of the edge atoms greatly influence energetic parameters of the covalent bonding as seen in Table 5.3. The coupling energies $E_{\text{cpl}}^{\text{tot}}$ related to the addition to zigzag and armchair edges of single-H-terminated graphene decrease more than twice by value. At the same time, addition to the basal plane is accompanied by more than twice increase in the value. The double termination of the graphene edge atoms causes the transformation of the

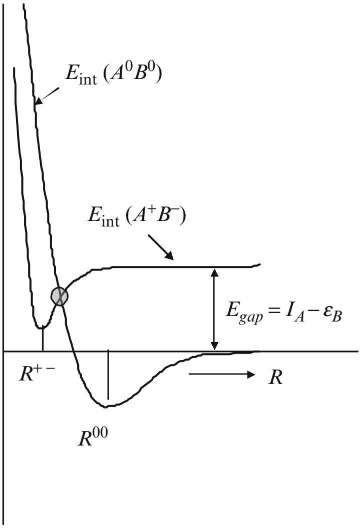

Fig. 5.19 Scheme of terms of an IMI potential of type 3 (Sheka 2011a). (A^0B^0) and (A^+B^-) match the term branches related to the IMI between neutral molecules and their ions, respectively

endothermic reaction for GNB 6 into the exothermic one for GNB 7 that needs for its completion ~2 kcal/mol thus showing that the IMI is not described more by the potential of type 1, presented in Fig. 5.1, but the potential of type 3 shown in Fig. 5.19 should enter the action.

Not only the change in the edge atom single-H-double-H termination causes that one in the IMI potential type, but a similar effect may be provided by increasing the size of the graphene single-H-terminated sheet. This is the case of GNB 8 formed by C_{60} covalently coupled with atoms on the basal plane of single-H-terminated (9, 8) nanographene (Fig. 5.20). A typical [2 + 2] cycloaddition forms the contact zone and the relevant coupling energy is high by value but positive. This means that in contrast to [C_{60} + (5, 5)] GNB, the creation of [C_{60} + (9, 8)] GNB requires energy while its stability depends on the high of the relevant barrier energy, which will be considered in the next section.

5.5.3 Energetic Parameters and Single-Reaction Barrier of Graphene Nanobuds

Looking for the reasons of so high changeability of GNBs forces to perform a comparative analysis of C_{60}-based composites, including $(C_{60})_2$, CNBs, and GNBs, at the level of energetic barriers. As was discussed in Sects. 5.3.2 and 5.4.3, it is quite reasonable to present the total coupling energy $E_{\mathrm{cpl}}^{\mathrm{tot}}$ related to GNBs consisting of two components, namely, $E_{\mathrm{def}}^{\mathrm{tot}}$ and $E_{\mathrm{chem}}^{\mathrm{tot}}$ that take the form

$$E_{\mathrm{def}}^{\mathrm{tot}} = E_{\mathrm{defgr}} + E_{\mathrm{def}\,C_{60}}, \qquad (5.9)$$

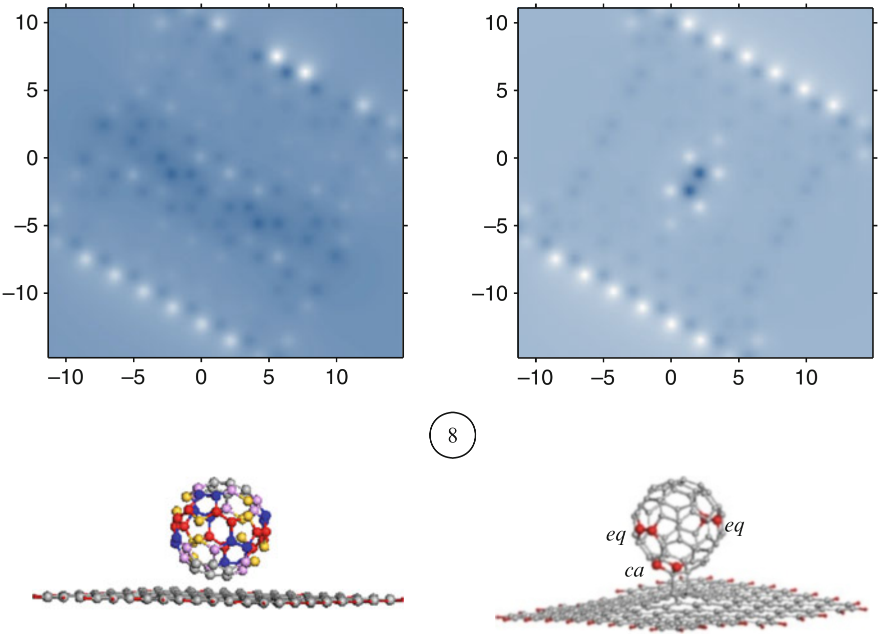

Fig. 5.20 [C_{60} + (9, 8)] graphene nanobud formed by attaching C_{60} fullerene to the basal plane of (9, 8) nanographene. Starting (*left*) and equilibrium (*right*) configurations with ACS maps (*above*) related to initial and perturbed graphene. *Red balls* on equilibrium structures point to fullerene atoms with the high-rank ACS values (Reproduced from Sheka and Shaymardanova (2011b), with permission from the Royal Society of Chemistry)

where

$$E_{\mathrm{defgr}}(R_{\mathrm{CC}}) = \Delta H^{\mathrm{op}}_{\mathrm{NGr/GNB}}(R_{\mathrm{CC}}) - \Delta H^{\mathrm{eq}}_{\mathrm{NGr}} \tag{5.10a}$$

and

$$E_{\mathrm{def\,C_{60}}}(R_{\mathrm{CC}}) = \Delta H^{\mathrm{op}}_{\mathrm{C_{60}/GNB}}(R_{\mathrm{CC}}) - \Delta H^{\mathrm{eq}}_{\mathrm{C_{60}}}. \tag{5.10b}$$

Here, $\Delta H^{\mathrm{op}}_{\mathrm{NGr/GNB}}(R_{\mathrm{CC}})$ and $\Delta H^{\mathrm{op}}_{\mathrm{C_{60}/GNB}}(R_{CC})$ present heats of formation of the one-point-geometry configurations of the NGr and fullerene components of the equilibrium configurations of the studied GNB characterized by the intermolecular distance R_{CC}. Accordingly, the chemical contribution into the coupling energy can be determined following (5.7). Figure 5.21 presents the dependence of $E^{\mathrm{tot}}_{\mathrm{cpl}}(R_{\mathrm{CC}})$, $E^{\mathrm{tot}}_{\mathrm{def}}(R_{\mathrm{CC}})$, and $E^{\mathrm{tot}}_{\mathrm{chem}}(R_{\mathrm{CC}})$ on the intermolecular 1–1′ and 2–2′ C–C distances (see Fig. 5.3a) for GNB 8. The three plottings in the figure are generally similar to those presented in Fig. 5.4 and Fig. 5.13 related to the $(C_{60})_2$ dimer and [C_{60} + (4, 4)] CNB. This is obviously resulted from the similarity of atomic structure of the contact zones formed in all the considered cases by [2 + 2] cycloadditions. The coupling

Fig. 5.21 Profile of the barrier of the $[C_{60} + (9,8)]$ GNB decomposition (GNB 8) (Reproduced from Sheka and Shaymardanova (2011b), with permission from the Royal Society of Chemistry). *1.* $E_{\mathrm{cpl}}^{\mathrm{tot}}(R_{\mathrm{CC}})$; *2.* $E_{\mathrm{def}}^{\mathrm{tot}}(R_{\mathrm{CC}})$; *3.* $E_{\mathrm{chem}}^{\mathrm{tot}}(R_{\mathrm{CC}})$ (see text)

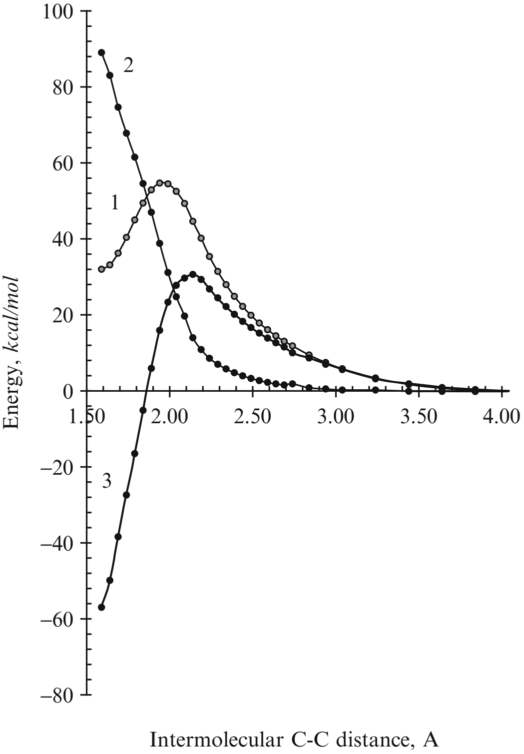

energy $E_{\mathrm{cpl}}^{\mathrm{tot}}$ can be evidently divided into $E_{\mathrm{def}}^{\mathrm{tot}}$ and $E_{\mathrm{cov}}^{\mathrm{tot}}$ components of the same type as those related to the previous two cases. However, the difference in numerical values of the two components at starting point results in a remarkable lifting of the $E_{\mathrm{cpl}}^{\mathrm{tot}}(R_{\mathrm{CC}})$ minimum for GNB 8 moving it into positive energy region. Consequently the barrier energy $E_{\mathrm{barr}}^{\mathrm{GNB}}$ lowers up to 22.7 kcal/mol. Here again we are facing a peculiar feature that cannot be explained by other things than the topochemistry involved in the addition reaction C_{60} + NGr.

5.6 The Identity of [2 + 2] Cycloadditions and Topochemistry of Addition Reactions

The discussed nanobuds, including C_{60} oligomers, CNBs, and GNBs, are resulted from a single-reaction covalent pair-pair bonding between the components, where each of the latter delegates a pair of the most chemically active atoms to form intermolecular junctions. The formed nanobuds present a rather complicated set of covalently bound composites that differ by both coupling energies and the structure of intermolecular junctions. Thus, only $(C_{60})_2$ dimer, sidewall CNBs,

Table 5.4 Joint characteristics of the nanobud [2 + 2] cycloadditions

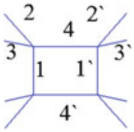

	C–C bonds, Å[a]						
Nanobuds	1	2	3	4	N_{DA}[b], e	E^{tot}_{chem}, kcal/mol	E^{NB}_{barr}, kcal/mol
$C_{60} + C_{60}$[c]	1.548	1.515	1.515	1.596	0.271, 0.271	−112.97	65.24
	1.548	1.516	1.516	1.596			
CNB 3[d]	1.567	1.483	1.486	1.652	0.308, 0.307	−134,31	–
	1.567	1.520	1.518	1.590			
CNB 5[d]	1.566	1.484	1.486	1.652	0.305, 0.304	−78,59	36.07
	1.566	1.520	1.518	1.590			
GNB 3[e]	1.591	1.496	1.496	1.581	0.183, 0.173	−98,91	–
	1.591	1.519	1.518	1.579			
GNB 6[e]	1.589	1.493	1.494	1.578	0.216, 0.201	−124,11	–
	1.589	1.519	1.517	1.580			
GNB 7[e]	1.590	1.492	1.492	1.578	0.189, 0.165	−60,42	–
	1.589	1.517	1.519	1.580			
GNB 8[f]	1.591	1.494	1.494	1.576	0.227, 0.174	−56.98	22.70
	1.592	1.519	1.518	1.580			

Reproduced from Sheka and Shaymardanova (2011b), with permission from the Royal Society of Chemistry

[a] The bond numeration corresponds to the insert. Two-row presentation distinguishes the primed bonds (the second rows) related to C_{60} in all cases from unprimed ones (the first rows) related to the C_{60} partner

[b] The data are related to the pair of atoms of C_{60} partners in the nanobuds. The data for fullerene partner are presented in the first cell

[c] C_{60} dimer

[d] [C_{60} + (4,4)] CNB. CNB′ numbering corresponds to that in Figs. 5.7 and 5.9

[e] [C_{60} + (5,5)] GNB. GNB′ numbering corresponds to that in Figs. 5.14 and 5.17

[f] [C_{60} + (9,8)] GNB (see Fig. 5.18)

and basal plane GNBs can be characterized by the [2 + 2] cycloaddition as alike intermolecular junction. Table 5.4 summarizes data covering these three cases.

As seen in the table, structural characteristics concerning the [2 + 2] cycloadditions are practically identical within CNB and GNB groups while the coupling energies differ therewith quite considerably. Obviously, the observed feature is a convincing manifestation of the topological nature of the reaction considered. However, nowadays there is a lack of appropriate concepts and terms that could interconnect methodologies of quantum chemistry and chemical topology at a quantitative level so that we have to stay among habitual chemical ideas as well to try to find among them those points that may indicate the difference in topology. Thus, within the framework of single-reaction approach, one of the first attempts to interpret topological peculiarities in the terms of usual application was made by Haddon (1993) who suggests the dependence of chemical activity of *sp*^{2} nanocarbons on the curvature of the carbon skeleton. However, as thoroughly shown later (Sheka and

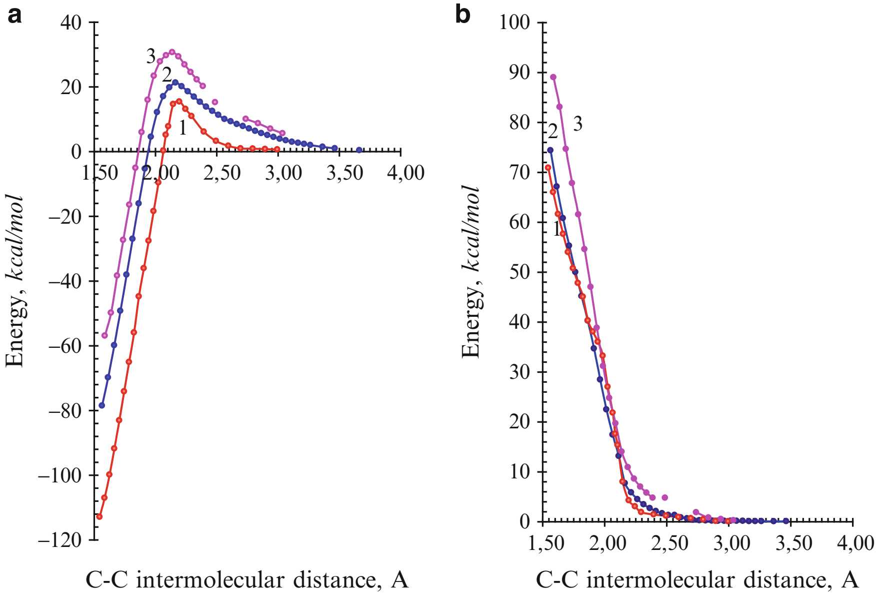

Fig. 5.22 $E^{tot}_{cov}(R)$ (**a**) and E^{tot}_{def} (**b**) plottings for $(C_{60})_2$ dimer (*1*), [C_{60} + (4, 4)] CNB 5 (*2*), and [C_{60} + (9, 8)] GNB 8 (*3*) (Reproduced from Sheka and Shaymardanova (2011b), with permission from the Royal Society of Chemistry)

Chernozatonskii 2007), the Haddon approach is quantitatively supported in rare cases only, that is why the approach based on simultaneous consideration of covalent coupling and deformation suggested later (Sheka and Shaymardanova 2011b) seems to open up much larger possibilities in describing chemical modification of sp^2 nanocarbons. According to the latter, the discussed inconsistence of changeable energetic characteristics with the identity of the intermolecular [2 + 2] cycloaddition junctions may be addressed to a specificity of the intermolecular interaction between the components of the nanobuds.

The specificity concerns two facets related to covalent bonding in the contact area and to the deformation of carbon skeletons. Characterized by $E^{tot}_{cov}(R_{CC})$ and $E^{tot}_{def}(R_{CC})$, respectively, a comparative presentation of the considered composites is shown in Fig. 5.22. As mentioned earlier, $E^{tot}_{cov}(R_{CC})$ curves present barrier profiles in terms of DA-assisted intermolecular interaction schematically shown in Figs. 5.1 and 5.19. The energy gap $E_{gap} = I_A - \varepsilon_B$ is of key importance for the case, so that changing in either ionization potential or electron affinity of partners may influence both the depth of the energy minimum at R^{+-} and the barrier high. Table 5.5 summarizes the relevant data for the studied nanobuds. The energy E_{gap} is different due to decreasing ionization potential when going from C_{60} fullerene to graphene (9.87, 9.19, and 8.2 eV for C_{60}, (4, 4) SWCNT, and (9, 8) NGr, respectively). In the latter case, the ionization potential depends on both the graphene sheet size and the edge saturation and constitutes ~8.5 ± 0.2 eV in the case of non-saturated edges. Energies E^{tot}_{cov} and E_{barr} synchronously follow the E_{gap} changes, decreasing by the

Table 5.5 Parameters of donor–acceptor interaction in C_{60}-based nanobuds

Nanobud	E_{gap}, eV	$E_{\text{cov}}^{\text{tot}}$, kcal/mol	E_{barr}, kcal/mol	Charge, e C_{60}	Partner 2
$(C_{60})_2$	7.21	−112.97	15.36	0	0
CNB 5	6.53	−78.59	21.22	−0.028	0.028
GNB 8	5.54	−56.99	30.62	−0.092	0.092

Reproduced from Sheka and Shaymardanova (2011b), with permission from the Royal Society of Chemistry

absolute value in the former case thus lowering the barrier. The gap decreasing promotes a significant charge transfer between the nanobud components in the ground state as well. Therefore, data presented in Fig. 5.22a and Table 5.5 reveal changes in the DA interaction in the studied nanobuds that significantly influence the covalent bonding in the relevant [2 + 2] cycloadditions.

As for deformation energies, those presented in Fig. 5.22b show quite similar dependence on the spacing between nanobuds components, differing only in the near vicinity of the relevant cycloadditions. For the latter, the energies constitute 70.83, 74.33, and 88.98 kcal/mol related to $(C_{60})_2$, CNB 5, and GNB 8, respectively, thus highlighting the growth of the difficulty to adopt the structure of the carbon skeleton to the sp^2–sp^3 transformation caused by the formation of [2 + 2] cycloaddition when going from fullerene to CNT and graphene.

Still open there has been a question concerning topological effects on odd-electron system of graphene. An obvious consequence concerns a suspected non-locality of the contact zone of GNBs. Last examinations have revealed a clearly seen non-superpositional character of multiple additions to a single graphene sheet (Sheka 2012, unpublished). A triple $[(C_{60})_3 + (9, 8)]$ GNB with single-H-terminated edge atoms is shown in Fig. 5.23 in two projections. The molecules are attached to the basal plane of the sheet as well as to the armchair and zigzag edges. As turned out, the coupling energy of this bud deviates drastically from a sum of the coupling energies related to three single GNBs that correspond to the attachments mentioned above. Moreover, it was shown that after decomposition of both the triple GNB as well as of the three different single GNBs, the graphene sheet is characterized by lower energy in comparison with that of pristine one. Therefore, the addition of fullerene provokes a structural transition in the substrate thus revealing a nonstability of the pristine structure. The structural nonstability seems to be a characteristic feature of a large graphene sheet that greatly complicates the consideration of topology effects, if not only these effects manifestation.

5.7 Graphene + Carbon Nanotube Composites

All the above-considered composites can be attributed to the composites with a single contact that was provided by the peculiarities of the C_{60} fullerene. In the case of CNT + graphene composites, we are facing the situation with multiple

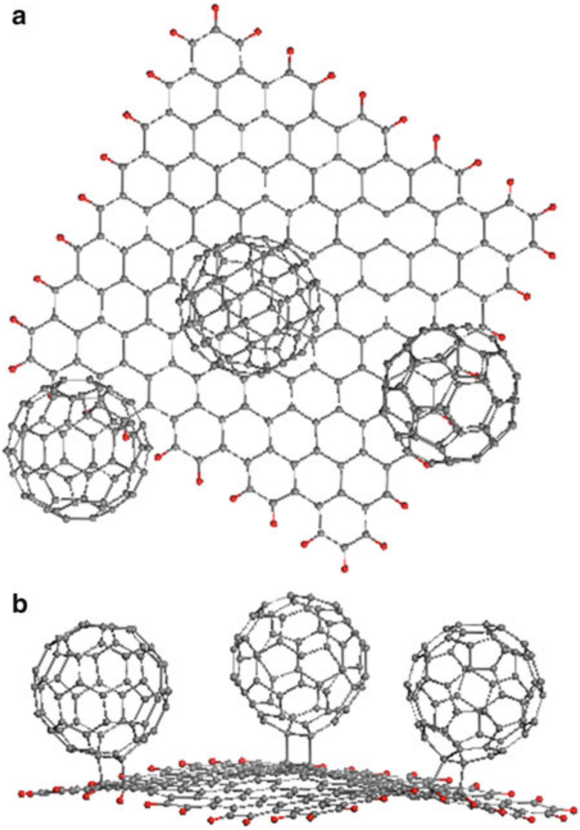

Fig. 5.23 Equilibrium structure of a triple $[(C_{60})_3 + (9, 8)]$ GNB in *top* (**a**) and *side* (**b**) views (Sheka 2012, unpublished)

contacts in each case due to extreme specificity of both components (Sheka and Chernozatonskii 2010a). Therefore, the composites form the platform for elucidation the topochemical character of the interaction between spatially extended species.

As previously, both components are good donors and acceptors of electrons (Sheka and Chernozatonskii 2010b, c, d), so that the IMI between them is subordinated to two-well shape of the ground state energy term shown in Figs. 5.1 and 5.19. This provides the formation of two modes of composites, one of which consists of weakly interacting components $A + B$ located at comparatively large distance while the second AB is formed in the range of short interatomic distances and corresponds to strongly coupled composition.

The next point concerns the obvious difference in the structure of contact zones of the composites, in contrast to C_{60}-carbon and C_{60}-graphene nanobuds, where the contact zones were limited to [2 + 2] cycloadditions. In view of a considerable electron correlation in both species, the formation of contact zones between them is subordinated to not only point high-rank ACS, as previously, but the ACS high-rank profiles over sets of atoms from both sides.

The third complication concerns a great variety of multi-derivative structures, which can be formed, when both tubes and graphene serve either as main bodies or present attached additives. The first attempt to consider properties of these complicated structures has been undertaken in Sheka and Chernozatonskii (2010a). Computed profiles of the atomic chemical susceptibility (ACS) along the tube and across their body as well as over NGr sheets served as quantified pointers that allowed localizing the most active contact zones of interacting partners.

To make the presented below more clear, let us remind peculiarities of the ACS distributions of both partners that allow for predicting addition reactions to be expected. While, on the subject of carbon nanotubes, we must take into account the following (Sheka and Chernozatonskii 2010b):

- The space of chemical reactivity of SWCNTs coincides with the coordinate space of their structures while different for the particular structure elements. This both complicates and facilitates chemical reactions involving the tubes depending on a particular reaction goal.
- Local additions of short-length addends (involving individual atoms, simple radical, and so forth) to any SWCNT are the most favorable at open empty ends, both armchair and zigzag ones, the latter more effective. Following these places in activity are cap ends, defects in the tube sidewall, and sidewall itself. The reactivity of the latter is comparable with the highest reactivity of fullerene atoms.
- Chemical contacts of SWCNTs with spatially extended reagents (graphene sheets) can occur in three ways: namely, when the tube is oriented either normally or parallel to the surface and when graphene acts as a “cutting-blade” to the tube sidewall.
- Addition reactions with the participation of multi-walled CNTs will proceed depending on the target atoms involved. If empty open ends of the tubes are main targets, the reaction will occur as if one deals with an ensemble of individual SWCNTs. If sidewall becomes the main target of the reaction, output will depend on the accessibility of inner tubes additionally to the outer one.

A concentrated view on the reactivity of atoms of a rectangular NGr presented in Fig. 5.14 allows for stating that (Sheka and Chernozatonskii 2010c):

- Any chemical addend will be firstly attached to the NGr zigzag edges, both hydrogen-terminated and empty.
- Slightly different by activity non-terminated armchair edges compete with zigzag ones.
- Chemical reactivity of basal atoms only slightly depends on the edge termination and is comparable with that of SWCNT sidewall and fullerenes, thus providing a range of addition reactions at the NGr surface.
- The disclosed chemical reactivity of both edges and the main body of NGr causes a particular two-mode pattern of the NGr attaching to any spatially extended molecular object such as either CNT or substrate surface, namely, a normal mode and a tangent or parallel one.

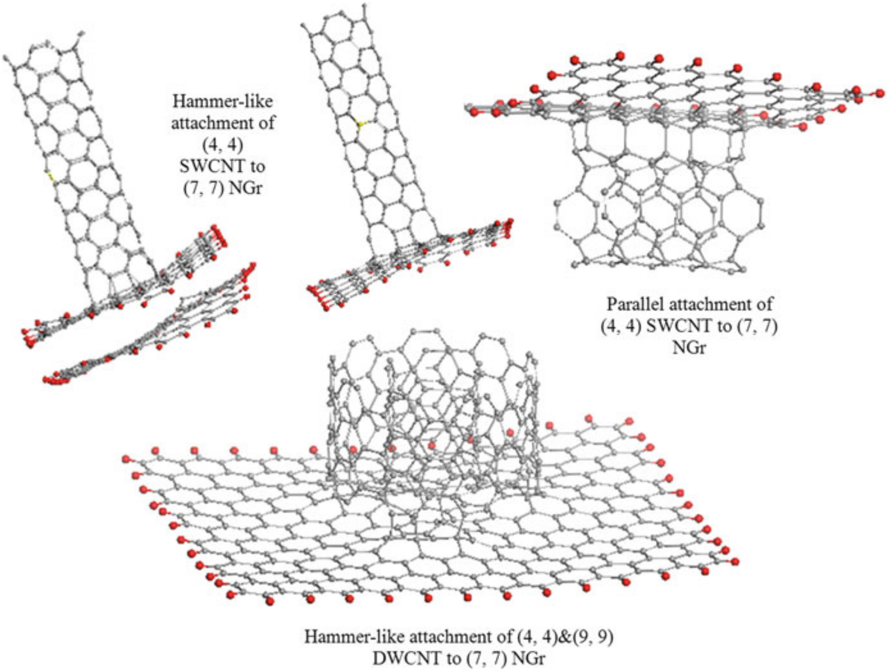

Fig. 5.24 Equilibrium structures of CNT + NGr composites

Two SWNT fragments presenting (n, n) and (m, 0) families, namely, (4, 4,) and (8, 0) and a set of NGrs of different size are chosen to reveal general tendencies of the composite formation (Sheka and Chernozatonskii 2010a). Due to the fact that the space of chemical reactivity of both CNTs and graphene coincides with the coordinate space of their structures, even single addition reactions, which lead to the composite formation, are not local but are largely extended in the space. This greatly complicates the construction of starting dyads, triads, and more complex configurations of components making their number practically endless. However, a thorough analysis of the ACS profiles of both components made it possible selecting two main groups of the composites, conditionally called "hammer" and "cutting-blade" structures. The former follows from the fact that empty ends of SWCNTs are the most chemically active so that the tubes might be willingly attached to any NGr forming a hammer handle. The latter is a consequence of exclusive chemical reactivity of both zigzag and armchair edges of non-terminated NGr, so that NGr can touch a SWCNT sidewall tangentially as a blade.

Figure 5.24 briefly sums up the main features that accompany the attachment of CNT to the basal plane of graphene in the hammer-like manner. The formation of composites significantly disturbs the NGr plane due to sp^2–sp^3 transformation of its carbon atoms involved in the contact zone, and this transformation is transferred even to the second layer of graphene. When the tube is oriented parallel to the plane, the equilibrium structure occurs to depend on whether the tube open ends are either empty or terminated (say, by hydrogens). In the first case, the tube and the NGr attract each other willingly and seven newly formed intermolecular C–C bonds provide the tight connection between the partners. When tracing subsequent steps of the joining (optimization) (Sheka and Chernozatonskii 2010a), one can see that the coupling starts at the tube ends by the formation of single bonds at first and then a pair of the C–C bonds at each end. Afterwards, these bonds play the role of the strops of gymnastic rings that pull the tube body to the sheet. However, when the tube ends are hydrogen-terminated, no intermolecular C–C bonds are formed, and the total energy coupling energy becomes repulsive.

The fragment of a double-wall CNT (DWCNT) in Fig. 5.24 consists of fragments of (4, 4) and (9, 9) SWCNTs with the same number of benzoid units along the vertical axis and open empty ends on both sides. Owing to the slightly different periodicity of the Kekule-incomplete Clar-complete Clar networks (Matsuo et al. 2003) in the two tubes, the fragment lengths do not coincide exactly. In due course of the optimization, the attachment of the joint fragment to the graphene sheet starts from the formation of intermolecular C–C bonds with either inner or outer tube depending on which is closer to the sheet. When opposite free ends of the tube are not fixed, the remaining fragment slides outwards, transforming the composition into a peculiar "telescope" system. When the free ends are fixed, both inner and outer fragments are joined to the sheet as shown in the figure. The coupling energy is large enough to provide a strong coupling between the graphene sheet and the DWCNT that explains a high stability of recently synthesized MWCNTs-graphene composite under conditions when one end of each MWCNT was fixed (Kondo et al. 2008).

Analyzing the presented data, it makes possible to conclude the following (Sheka and Chernozatonskii 2010a):

1. The normal attachment of an empty-end SWCNT to graphene sheet is energetically favorable.
2. The horizontal attachment of the tube is also possible while much weaker.
3. H termination of the tube ends renders the horizontal attachment impossible and severely weakens the normal one.
4. Both multiple normal attaching of SWCNTs and a single and multiple attaching of a DWCNT are energetically favorable, and graphene sheets can be easily fixed over tubes in case their open ends are empty.
5. Graphene sheets are extremely structure flexible and even a weak intermolecular interaction causes a loss of the sheet flatness.

Cutting-blade composites are shown in Fig. 5.25. Two SWCNT fragments, namely, (8, 0) and (4, 4), as well as (7, 7) NGr were chosen to demonstrate typical compositions to be formed in this case (Sheka and Chernozatonskii 2010a). At start each time, the NGr edge was oriented parallel to the cylinder axis in the vicinity of SWCNT along a line of sidewall atoms in such a way to maximize the number of intermolecular C–C contacts. Since ACS distribution over the cross-sectional atoms of both tubes is well homogeneous (Sheka and Chernozatonskii 2010b), there is no azimuthal selectivity of the line position in this case. As for NGrs,

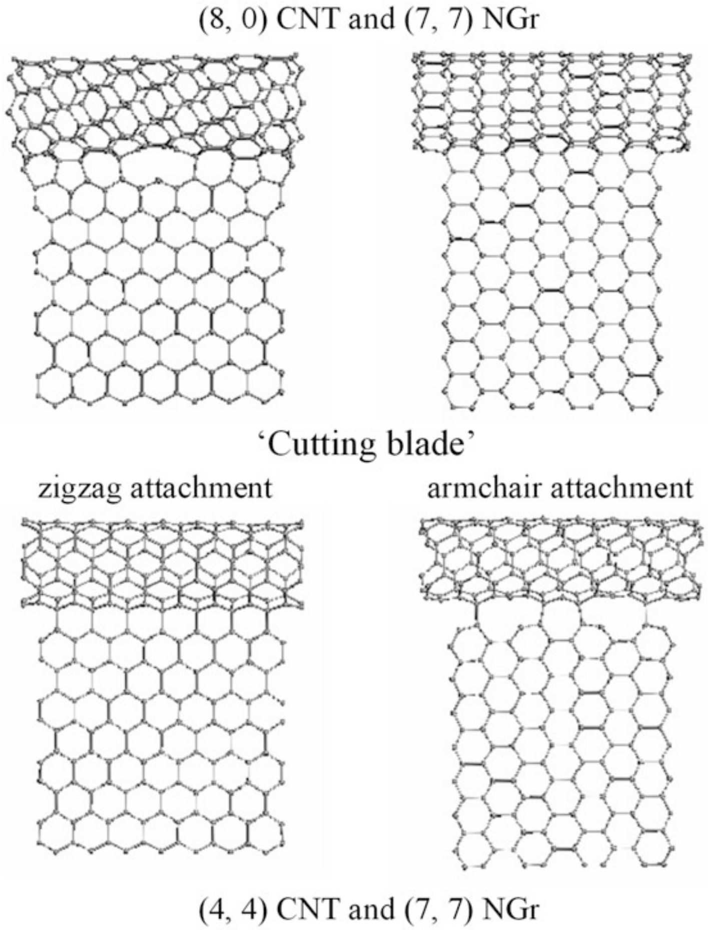

Fig. 5.25 Equilibrium structures of cutting-blade CNT + NGr composites

zigzag and armchair edges of NGr with empty edges are comparable (see Fig. 5.14) while somewhat different. Due to this, two NGr orientations with respect to the tube sidewall were examined. Basing on the coupling energy, the preference in the cutting-blade structures should be given to armchair attachment in the case on (8, 0) SWCNT while the zigzag attachment is preferential for (4, 4) SWNT.

Since the cutting-blade attachment disturbs the ACS distribution along the line of atoms involved in the contact only, a multiple addition of the graphene sheets is possible, whose number is governed by sterical constrains mainly. Figure 5.26 presents a set of such dicomposites. Obviously, for large-diameter tubes, a sequential addition of a number of NGr will result in the formation of a multi-tooth gear. A particular attention should be drawn to a cradle-like composite shown in the figure. It may be considered as the illustration of a possible fixation of an individual

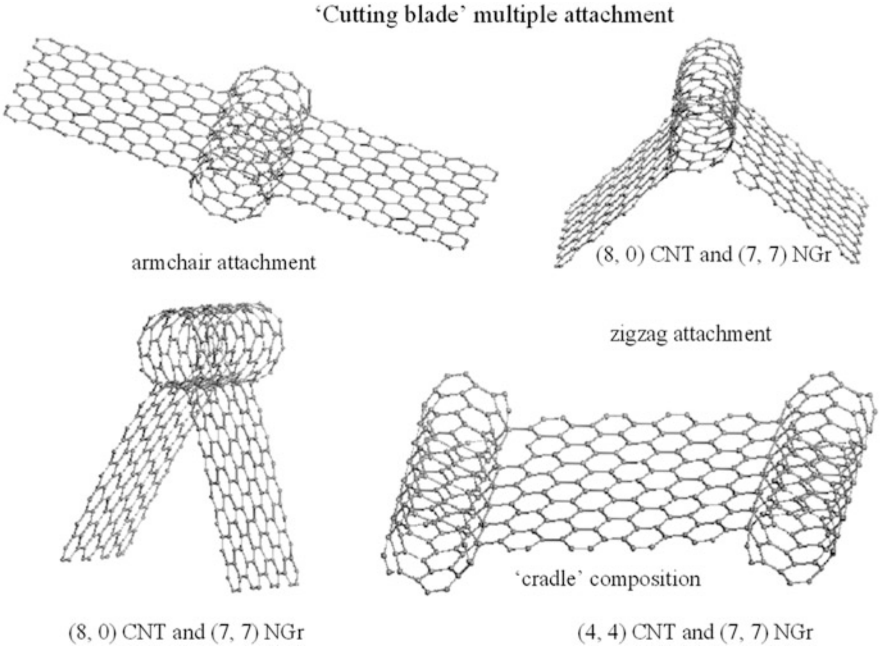

Fig. 5.26 Equilibrium structures of CNT + NGr dicomposites

graphene sheet under conditions of the least perturbation of the sheet. Obviously, not (4, 4) SWCNT but much larger tubes should be taken as supporters. Since ACS of SWCNTs depends on the tube diameter only slightly (Sheka and Chernozatonskii 2010b), the cradle composite formation can be provided by any tubes, even different in diameter within the pair.

In spite of the doubtless exemplary of studied composites (Sheka and Chernozatonskii 2010a), the performed investigations allowed making the following general conclusions:

1. The formation of the hammer and cutting-blade composites is energetically favorable not only as mono-addition of NGr to the tube body and vice versa but a multi-addend attachment, as well.
2. A strong contact between the tube and NGr is provided by the formation of an extended set of the intermolecular C–C bonds, number of which is comparable with the number of either tube end or NGr edge atoms.
3. The contact strength is determined by both the energy of the newly formed C–C bonds and their number. Optimization of the latter dictates a clear preference towards zigzag or armchair edges of the attaching NGr depending on the tube configuration. Thus, (8, 0) SWCNT (as all other members of the (m, 0) family) prefers armchair contacts that maximize the number of point contacts. In its turn, (4, 4) SWCNT (as well as other members of the (*n*, *n*) family) favors zigzag contacts due to the same reason.

4. The total coupling energy between the NGr addend and tube involves both the energy of the C–C bond formed and the energy of deformation caused by the reconstruction of sp^2 configuration for the carbon atom valence electrons into sp^3 one. It can be thought that the latter depends on the tube diameter. However, the data are so far rather scarce, and an extended investigation of the problem is needed.
5. In general, the coupling energy of cutting-blade composites is much more than that of hammer ones, which is important for practical realization of the composites production
6. The final product will depend on whether both components of the composition are freely accessible or one of them is rigidly fixed. Thus, in diluted solutions where the first requirement is met, one can expect the formation of cutting-blade composites due to significant preference in the coupling energy. Oppositely, in gas reactors where often either CNTs or graphene sheets are fixed on some substrates, the hammer composites will be formed as it has been shown just recently (Kondo et al. 2008; Chen et al. 2011).
7. All the mentioned peculiarities provide an extremely large field for a detailed study of different topological effects.

5.8 Topochemical Character of the Graphene Hydrogenation

5.8.1 General Design of the Graphene Hydrogenation

As has been revealed just recently, a significant correlation of odd electrons of graphene strongly influences its chemical modification, the hydrogenation, in particular (Sheka and Popova 2012a, b). The hydrogenation has been considered in a manner of consequent single reactions subordinated to a stepwise addition of hydrogen atoms to a double-H-terminated (5, 5) NGr membrane shown in Fig. 5.14c, alongside with the corresponding ACS map. Two initial states of the membrane are considered related to either fixed (fixed membrane) or unrestricted motion (free-standing membrane) of the carbon atoms situated over the membrane perimeter. The perimeter atom fixation implies that the relevant atoms are excluded from the optimization procedure at further steps of a consequent hydrogenation. The stepwise addition of hydrogen to membranes is subordinated to a particular algorithm described in details in Sheka (2011a) that is governed by the highest ACS of the carbon atoms, calculated at every step of the reaction.

Both the hydrogenation of graphene itself and the final hydrides formed depend on several external factors, namely, (1) the state of the fixation of the membrane, (2) the accessibility of the substrate sides to hydrogen, and (3) molecular or atomic composition of the hydrogen vapor. These circumstances make both computational consideration and technology of the graphene hydrogenation multimode with the number of variants not fewer than eight if only molecular and atomic adsorption does not occur simultaneously. The study (Sheka and Popova 2012a, b) has involved all the hydrogenation modes related to atomic adsorption and to two modes of the molecular adsorption. Taking together, the results allow for suggesting a rather integral picture of the events that accompany hydrogenation of graphene. It is summed up in Table 5.6. Additionally to the general picture, the following answers to crucial questions related to the hydrogenation of graphene were suggested.

1. *Which kind of the hydrogen adsorption, namely, molecular or atomic, is the most probable?*

Following from Table 5.6, the study has convincingly shown that only atomic adsorption is effective and energetically favorable, which is consistent with a widely known fact of a practical absence of molecular hydrogen adsorption on graphite. It is important to note that the reason has a direct relation to the main topic of this chapter.

As for atomic adsorption, the formation of hydrides with practically total covering of the basal plane occurs quite possibly. When both sides of the membrane are accessible to hydrogen atoms, the hydrogenation of NGr is completed by the formation of the 100 % covered regularly structured provided with chair-like cyclohexanoid units (Fig. 5.27a). If the membrane is accessible from one side only, the consequent attachment of hydrogen atoms to the substrate causes arching of its carbon skeleton that takes the shape of a canopy at the final stage (Fig. 5.27b). In both cases, C–C bonds lengthen taking 1.51–1.53 Å. However, under fixation of the membrane edges, not all the bonds are able to meet the requirement so that a part of them should stay quite short. Under this condition, a pair of hydrogen atoms, which had to be attached to two carbon atoms forming the bonds, is not allowed to perform the job thus stimulating atoms to associate and to form a hydrogen molecule outside of the basal plane. As seen in Fig. 5.27b, the last atoms 43 and 44 had such a fate, which resulted in desorption of one hydrogen molecule and lowering the plane covering up to 96 %.

At first glance, the final stage of the two-side adsorption of hydrogen atoms on the free-standing membrane (Fig. 5.27c) seems to be similar to that presented in Fig. 5.27a. However, attentive consideration reveals that the chair-like configuration of cyclohexanoids, regularly composed in the upper side of the sample, is violated when approaching the sample bottom so that we have to speak about the mixing of the cyclohexanoid conformers, which causes the distortion of the regular structure of the carbon skeleton. This circumstance does not prevent from achieving 100 % filling of the basal plane; nevertheless, the sample itself presents a mixture of a regular area neighboring with some elements of amorphous structure. Obviously, the partial contribution of each component depends on the graphene sample size.

In contrast to what has been said above, the one-side adsorption of the free-standing membrane has resulted in the formation of a peculiar basket that is formed when two ends of a rectangular figure situated over its diagonal are closely approached each other (Fig. 5.27d). The formation of the 100 % hydride of so peculiar shape is accompanied by the energy gain of ~1 kcal/mol per each carbon atom.

Table 5.6 Final products of the hydrogen adsorption on (5,5) nanographene

Atomic adsorption	Two-side access	One-side access	*Molecular adsorption*	Two-side access	One-side access
Fixed membrane	100 %-covered hydride of crystalline graphane structure (Fig. 5.27a)	96 %-covered hydride of canopy structure (Fig. 5.27b)	Fixed membrane	∼5 %-covered hydride of nonplanar sheet structure	No results
Free-standing membrane	100 %-covered hydride of crystalline graphane structure accompanied by fragments of amorphous structure (Fig. 5.27c)	100 %-covered hydride of a basket structure (see text) (Fig. 5.27d)	Free-standing membrane	10–15 %-covered hydride of irregular structure of bent sheet	No results

Reproduced from Sheka and Popova (2012b) with kind permission from Springer Science and Business Media

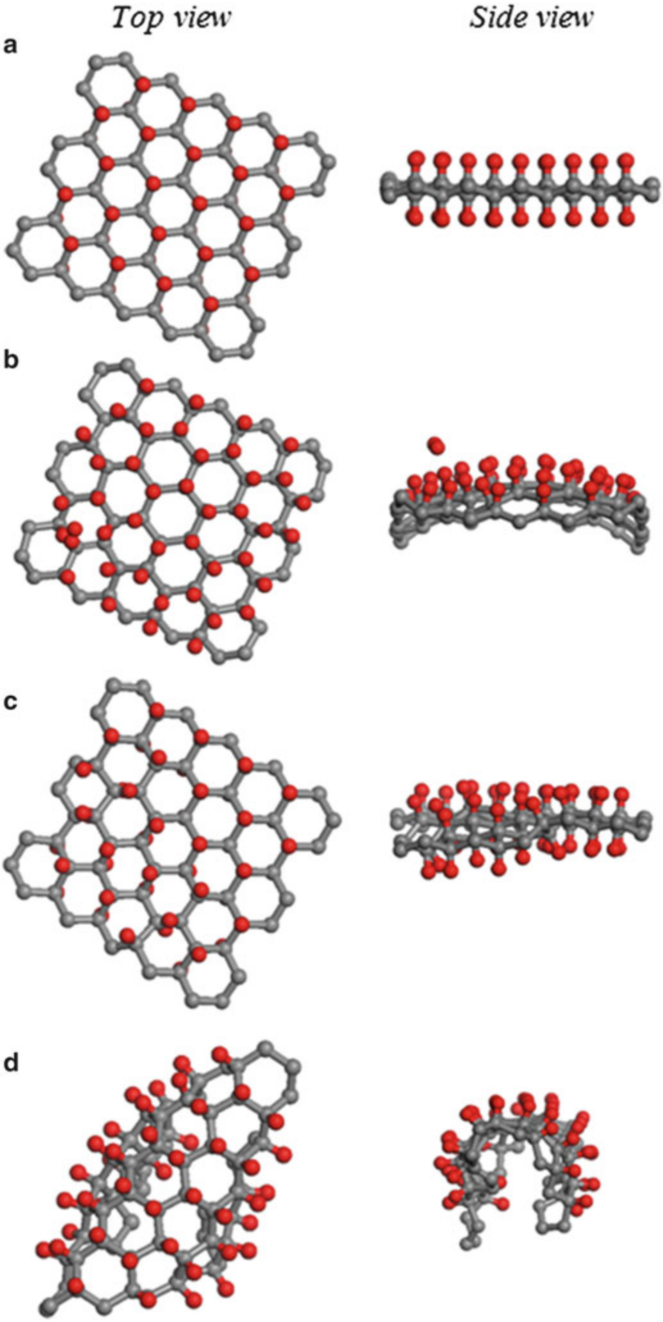

Fig. 5.27 *Top* and *side views* of the equilibrium structures of hydrides formed at the atomic adsorption of hydrogen on the fixed (**a**, **b**) and free-standing (**c**, **d**) (5,5) nanographene membrane, accessible to the adsorbate from both (**a**, **c**) and one (**b**, **d**) sides (Reproduced from Sheka and Popova (2012b), with kind permission from Springer Science and Business Media)

The reason for so dramatic difference between atomic and molecular adsorption has an evident topochemical nature and is a consequence of the tendency of the graphene substrate to conserve the hexagon pattern. But obviously, the pattern conservation can be achieved if only the substrate hydrogenation provides the creation of the cyclohexanoid structure that corresponds to either one of the conformers of the latter or their mixture. If non-coordinated deposition of individual atoms can meet the requirement, a coordinated deposition of two atoms on neighboring carbons of substrate evidently makes the formation of a cyclohexanoid-conformer pattern much less probable thus making molecular adsorption unfavorable.

2. *What is characteristic image of the hydrogen atom attachment to the substrate?*

The hydrogen atom is deposited on top of the carbon ones in both up and down configurations. In contrast to a vast number of organic molecules, the length of C–H bonds formed under adsorption exceeds 1.10 Å, therewith differently for different adsorption events. Thus, C–H bonds are quite constant by value of 1.122 Å in average for framing hydrogens that saturate edge carbon atoms of the substrate. Deposition on the basal plane causes enlarging the value up to maximum 1.152 Å (Sheka and Popova 2012a, b). However, the formation of a regular chair-like cyclohexanoid structure like graphane (Sofo et al. 2007; Elias et al. 2009) leads to equalizing and shortening the bonds to 1.126 Å. The above picture, which is characteristic for the fixed membrane, is significantly violated when going to one-side deposited fixed membrane or two-side deposited free-standing membrane that exhibits the difference in the strength of the hydrogen atoms coupling with the related substrates.

1. *Which carbon atom is the first target subjected to the hydrogen attachment?*

And

2. *How are carbon atoms selected for the next steps of the adsorption?*

Similarly to fullerenes and carbon nanotubes (Sheka 2011a), the formation of graphene polyhydrides $(CH)_n$ has been considered in the framework of single-reaction algorithmic stepwise computational synthesis, each subsequent step of which is controlled by the distribution of atomic chemical susceptibility in terms of fractional numbers of effectively unpaired electrons on atom, N_{DA}, of the preceding derivative over the substrate atoms. The quantity is a direct consequence of the odd-electron correlation. The high-rank N_{DA} values definitely distinguish the atoms that should serve as targets for a forthcoming chemical attack. Additionally, the lowest total energy criterion has provided the choice of the most energetically stable hydride. The successful generation of the polyderivative families of fluorides (Sheka 2010) and hydrides (Sheka 2011b) as well as other polyderivatives of fullerene C_{60} (Sheka 2011a), of 100 % polyhydride $(CH)_n$ related to chair-like graphane described above as well as ~96 % of table-like cyclohexanoid hydride $(CH)_n$ of the canopy shape, has shown a high efficacy of the approach in viewing process of the polyderivatives formation which makes it possible to proceed with a deep insight into the mechanism of the chemical modification.

3. *Is there any connection between the sequential adsorption pattern and cyclohexanoid conformers formed in due course of hydrogenation?*

The performed investigations have shown that there is a direct connection between the state of the NGr substrate and the conformer pattern of the polyhydride formed. The pattern is governed by the cyclohexanoid conformer whose formation under ambient conditions is the most profitable. Thus, a regular chair-like cyclohexanoid-conformed graphene with 100 % hydrogen covering, known as graphane (Sofo et al. 2007; Elias et al. 2009), is formed in the case when the NGr substrate is a perimeter-fixed membrane, both sides of which are accessible for hydrogen atoms. When the membrane is two-side accessible, but its edges are not fixed, the formation of a mixture of chair-like and boat-like cyclohexanoid patterns has turned out more profitable. As shown, the polyhydride total energy involves deformational and covalent components. That is why the difference in the conformer energy in favor of chair-like conformer formed in free-standing membrane is compensated by the gain in the deformation energy of the carbon carcass caused by the formation of boat-like conformer, which simulates a significant corrugation of the initial graphene plane. The mixture of the two conformers transforms therewith a regular crystalline behavior of graphane into a partially amorphous-like behavior in the latter case.

When the fixed membrane is one-side accessible, the configuration produced is rather regular and looks like an infinite array of *trans*-linked table-like cyclohexanoid conformers. The coupling of hydrogen atoms with the carbon skeleton is the weakest among all the considered configurations, which is particularly characterized by the longest C–H bonds of 1.18–1.21 Å in the length. The carbon skeleton takes a shape of a canopy exterior.

5.8.2 Energetic Characteristics Accompanying the Nanographene Hydrogenation

Total coupling energy that may characterize the molecule hydrogenation can be presented as

$$E_{\mathrm{cpl}}^{\mathrm{tot}}(n) = \Delta H_{n\,\mathrm{Hgr}} - \Delta H_{\mathrm{NGr}} - n\Delta H_{\mathrm{at}}. \tag{5.11}$$

Here $\Delta H_{n\,\mathrm{Hgr}}$, ΔH_{NGr}, and ΔH_{at} are heats of formation of graphene hydride with n hydrogen atoms, a pristine nanographene, and hydrogen atom, respectively. When one is mainly interested in the adsorption on basal plane, it is worthwhile to refer the coupling energy related to the basal adsorption to the energy of the framed membrane in the form

$$E_{\mathrm{cpl}}^{\mathrm{tot\ bs}}(k) = E_{\mathrm{cpl}}^{\mathrm{tot}}(k+44) - E_{\mathrm{cpl}}^{\mathrm{tot\ fr}}(44), \tag{5.12}$$

where $k = n - 44$ numbers hydrogen atoms deposited on the basal plane and $E_{\text{cpl}}^{\text{tot bs}}(k)$ presents the coupling energy counted off the energy of the framed membrane $E_{\text{cpl}}^{\text{tot fr}}(44)$.

The tempo of hydrogenation may be characterized by the coupling energy needed for the addition of each next hydrogen atom. Attributing the energy to the adsorption on the basal plane, the per step energy can be determined as

$$E_{\text{cpl}}^{\text{step bs}}(k) = E_{\text{cpl}}^{\text{tot}}(k + 44) - E_{\text{cpl}}^{\text{tot}}[(k + 44) - 1]. \tag{5.13}$$

Evidently, two main contributions, namely, the deformation of the fragment carbon skeleton (def) and the covalent coupling of hydrogen atoms with the substrate resulted in the formation of C–H bonds (cov), determine both total and per step coupling energies. Supposing that the relevant contributions can be summed up, one may evaluate them separately. Thus, the total deformation energy can be determined as the difference

$$E_{\text{def}}^{\text{tot}}(n) = \Delta H_{n\,\text{Hgr}}^{\text{sk}} - \Delta H_{\text{NGr}}. \tag{5.14}$$

Here, $\Delta H_{n\,\text{Hgr}}^{\text{sk}}$ presents the heat of formation of the carbon skeleton of the hydride at the nth step of hydrogenation, and ΔH_{NGr} presents the heat of formation of the initial graphene fragment. The value $\Delta H_{n\,\text{Hgr}}^{\text{sk}}$ can be obtained as a result of one-point-structure determination applied to the nth equilibrium hydride after removing all hydrogen atoms. Attributed to the basal plane, $E_{\text{def}}^{\text{tot}}(n)$ has the form

$$E_{\text{def}}^{\text{tot bs}}(k) = E_{\text{def}}^{\text{tot}}(k + 44) - E_{\text{def}}^{\text{tot fr}}(44). \tag{5.15}$$

Here, $E_{\text{def}}^{\text{tot fr}}(44)$ presents the deformation energy of the framed membrane.

The deformation energy, which accompanies each step of the hydrogenation, can be determined as

$$E_{\text{def}}^{\text{step bs}}(k) = \Delta H_{(k+44)\text{Hgr}}^{\text{sk}} - \Delta H_{[(k+44)-1]\text{Hgr}}^{\text{sk}}, \tag{5.16}$$

where $\Delta H_{(k+44)\text{Hgr}}^{\text{sk}}$ and $\Delta H_{[(k=44)-1]\text{Hgr}}^{\text{sk}}$ match heats of formation of the carbon skeletons of the relevant hydrides at two subsequent steps of hydrogenation.

Similarly, the total and per step chemical contributions caused by the formation of C–H bonds on the basal plane can be determined as

$$E_{\text{cov}}^{\text{tot bs}}(k) = E_{\text{cpl}}^{\text{tot bs}}(k) - E_{\text{def}}^{\text{tot bs}}(k) \tag{5.17}$$

and

$$E_{\text{cov}}^{\text{step bs}}(k) = E_{\text{cov}}^{\text{tot}}(k + 44) - E_{\text{cov}}^{\text{tot}}(k + 44 - 1). \tag{5.18}$$

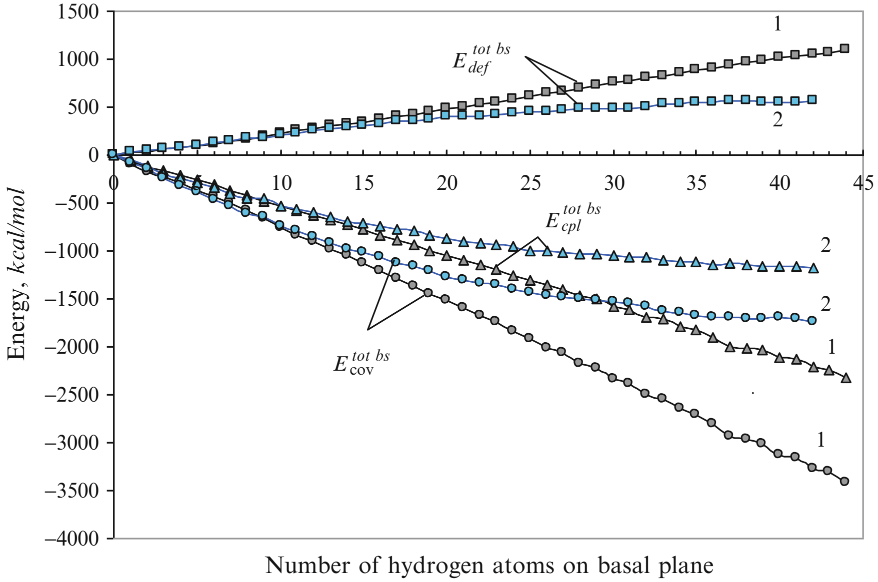

Fig. 5.28 Total energies of coupling $E_{\mathrm{cpl}}^{\mathrm{tot\ bs}}$ (*triangles*), deformation $E_{\mathrm{def}}^{\mathrm{tot\ bs}}$ (*squares*), and covalent bonding $E_{\mathrm{cov}}^{\mathrm{tot\ bs}}$ (*circles*) via the number of hydrogen atoms deposited on the basal plane for hydrides *1* (*dark gray*) and *2* (*light blue*) according to (5.13), (5.16), and (5.18), respectively

Figure 5.28 displays the calculated total energies for hydrides related to the fixed (1) and free-standing (2) membranes. The relevant per step energies are shown in Fig. 5.29. As seen in Fig. 5.28, the total energies $E_{\mathrm{cpl}}^{\mathrm{tot\ bs}}$ of both hydrides are negative by sign and gradually increase by the absolute value when the number of adsorbed atoms increases. Besides, the absolute value growth related to hydrides 2 is evidently slowing down starting at step 11 in contrast to the continuing growth for hydrides 1. This retardation is characteristic for other two energies presented in Fig. 5.28 thus quantitatively distinguishing hydrides 2 from hydrides 1. The growth retardation of both $E_{\mathrm{cpl}}^{\mathrm{tot\ bs}}$ and $E_{\mathrm{cov}}^{\mathrm{tot\ bs}}$ energies obviously shows that the addition of hydrogen to the fixed membrane of hydrides 2 at coverage higher than 30 % is more difficult than in the case of hydrides 1. This conclusion is supported by the behavior of per step energies $E_{\mathrm{cpl}}^{\mathrm{step\ bs}}$ and $E_{\mathrm{cov}}^{\mathrm{step\ bs}}$ plotted in Fig. 5.29a, c. If, in the case of hydrides 1, the energy values oscillate around steady average values of −52 and −72 kcal/mol for $E_{\mathrm{cpl}}^{\mathrm{step\ bs}}$ and $E_{\mathrm{cov}}^{\mathrm{step\ bs}}$, respectively, in the case of hydrides 2, $E_{\mathrm{cpl}}^{\mathrm{step\ bs}}$ oscillates around average values that grow from −64 to −8 kcal/mol. Similar $E_{\mathrm{cov}}^{\mathrm{step\ bs}}$ oscillations occur around a general level that starts at −88 kcal/mod and terminates at −8 kcal/mol (see Fig. 5.29c). Therefore, the reaction of the chemical attachment of hydrogen atoms to hydrides 1 is thermodynamically profitable through over the covering that reaches 100 % limit. In contrast, the large coverage for hydrides 2 becomes less and less profitable so that at final steps adsorption and desorption

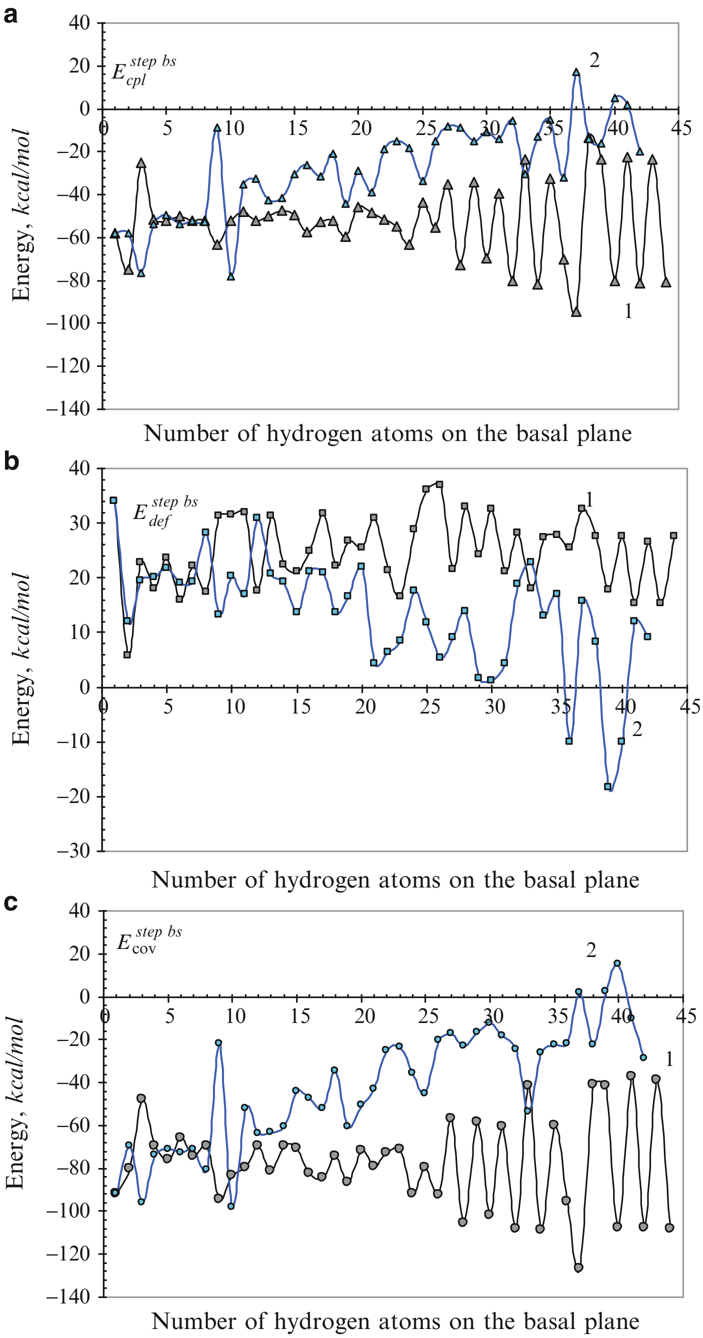

Fig. 5.29 Per step energies of coupling $E_{\text{cpl}}^{\text{step bs}}$ (**a**), deformation $E_{\text{def}}^{\text{step bs}}$ (**b**), and covalent bonding $E_{\text{cov}}^{\text{step bs}}$ (**c**) via the number of hydrogen atoms deposited on the basal plane for hydrides *1* (*dark gray*) and *2* (*light blue*) according to (5.13), (5.16), and (5.18), respectively

become competitive thus resulting in desorption of hydrogen molecules, which was described in the previous section.

An attention should be given to changing the deformation of the carbon skeleton caused by $sp^2 \rightarrow sp^3$ transformation of the carbon atom electron configuration. Gradually increased by value for both hydride families, the energy $E_{\mathrm{def}}^{\mathrm{tot\ bs}}$ shown in Fig. 5.28 describes strengthening the deformation in due course of growing coverage of the basal plane. Irregular dependence of $E_{\mathrm{def}}^{\mathrm{step\ bs}}$ on covering presented in Fig. 5.29b allows for speaking about obvious topochemical character of a multistep attachment of hydrogen atoms to the membrane basal plane.

5.8.3 Comparative View on the Hydrogenation of Fullerene C_{60} and Graphene

The topochemistry revealed above might imply, on the first glance, chemical reactions occurred in a space subordinated to restricting conditions like reactions on the solid surfaces (Schmidt 1971). However, one has to take into account the inherent topology of the graphene substrate that was mentioned in Sect. 5.1. If so and if the topology of graphene and fullerene is different, the hydrogenation seems to be the straight way to exhibit the difference.

Figure 5.30 present a summarized view on the consequent steps of the fullerene C_{60} stepwise hydrogenation, governed by the ACS algorithm, in due course of which a complete family of the C_{60} hydrides has been obtained (Sheka 2011b). When comparing the fullerene hydrides with those of graphene, one has to give the obvious preference to the graphene hydrides 2 obtained under the one-side adsorption on the basal plane of the fixed membrane. Energetic characteristics, which accompany the hydrogenation of fullerene C_{60} and (5, 5) NGr, are shown in Fig. 5.31. As seen in the figure, seemingly identical reactions are drastically different from the energy viewpoint. One may think that the final irregular hydrogen covering of hydrides 2 might be the reason for the difference. However, a comparison with the data related to hydrides 1, presented in Fig. 5.31, as well, not only does not improve the situation but significantly worsens it. It should be concluded that the hydrogenation has turned out a very indicative chemical procedure that has made the inherent difference in the topology of fullerenes and graphene the most impressive.

5.9 Inherited Topology and Deformation of Graphene

In this section we will consider a particular topological effect caused by the influence of the graphene edge termination on the inherited topology of the sheet. As turned out, the graphene deformation under external mechanical loading is extremely sensitive to the state of the sheet edge atoms and makes it possible to disclose a topological nature of this sensitivity.

Within the framework of the molecular theory, the response of nanographene sheet to external stresses is considered in terms of a mechanochemical reaction

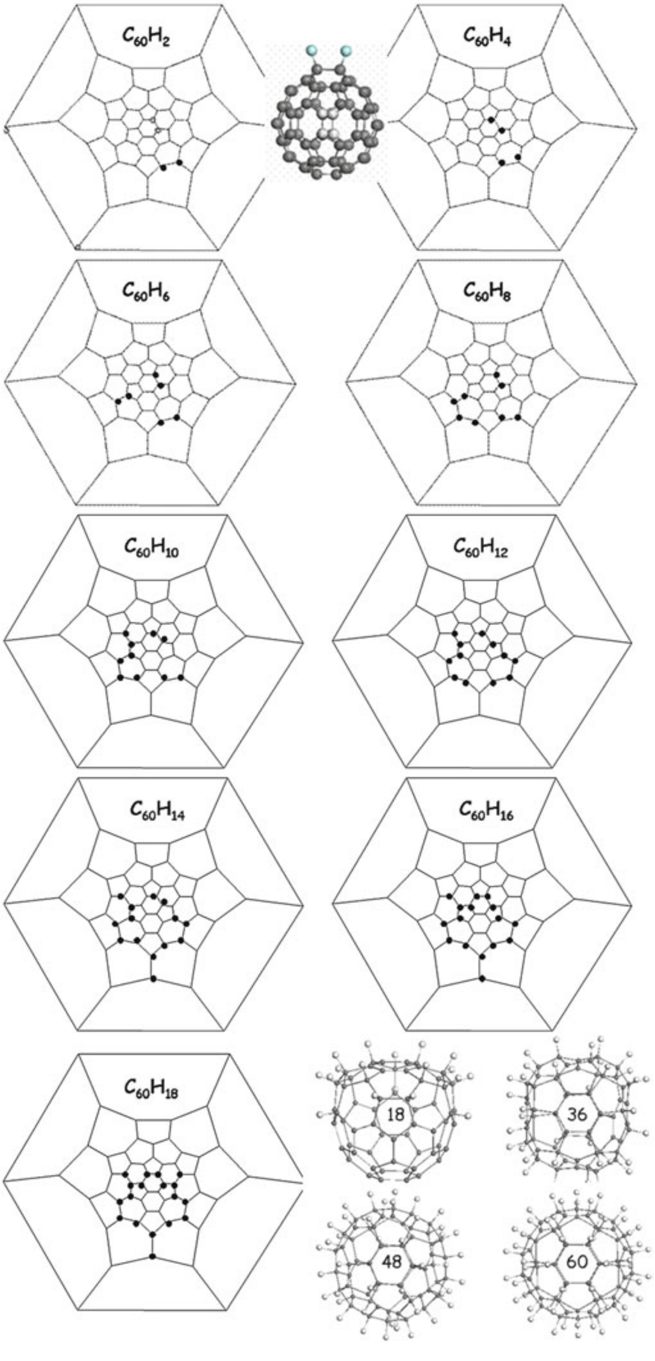

Fig. 5.30 Schlegel diagrams of successive steps of the C_{60} hydrogenation from $C_{60}H_2$ to $C_{60}H_{18}$ and atomic structures of $C_{60}H_{18}$, $C_{60}H_{36}$, $C_{60}H_{48}$, and $C_{60}H_{60}$ molecules (Reproduced from Sheka 2011b, with kind permission from Springer Science and Business Media)

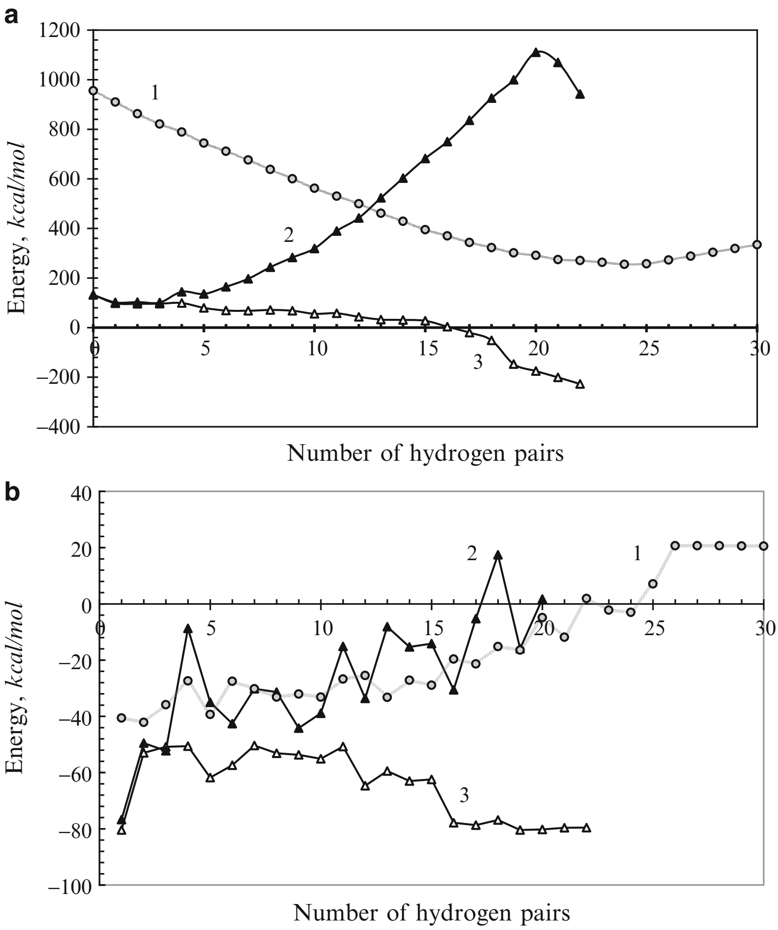

Fig. 5.31 Total energy (**a**) and per step coupling energy (**b**) for the families of C$_{60}$-fullerene hydrides (*curves* with *balls*), (5, 5) nanographene hydrides *1*(*curves* with *filled triangles*), and hydrides *2* (*curves* with *open triangles*)

(Sheka et al. 2011a, b). The quantum-chemical realization of the approach is based on the coordinate-of-reaction concept for the purpose of introducing a mechanochemical internal coordinate (MIC) that specifies a deformational mode (Nikitina et al. 1999). In the case of tensile deformation, the benzenoid pattern of graphene sheets and a regular packing of the units predetermined the choice of either parallel or normal MICs orientation with respect to the chain of C–C bonds. In the rectangular nanographene sheets and nanoribbons, the former orientation corresponds to tensile deformation applied to the zigzag edges (*zg* mode) while the latter should be attributed to the armchair edges (*ach* mode). The MIC configurations of the *ach* and *zg* tensile modes of the (5,5) NGr sheet are presented in Fig. 5.32. The deformation proceeds as a stepwise elongation of the MICs with the increment $\delta L = 0.1$ Å at each step so that the current MIC length constitutes $L = L_0 + n\delta L$, where L_0 is the initial length of the MIC and n counts the number of the deformation steps. Right ends of all the MICs are fixed so that these blue-colored atoms are immobilized while atoms on the left ends of MICs move along the arrows providing the MIC successive elongation, once excluded from the optimization as well. The relevant force of response is calculated as the energy gradient along the MIC, while the atomic configuration is optimized over all of the other coordinates under the MIC constant-pitch elongation.

Thus arranged computations revealed that a high stiffness of the graphene body is provided by the stiffness of benzenoid units. The anisotropy of the unit mechanical behavior in combination with different packing of the units either normally or parallel to the body C–C bond chains lays the ground for the structure-sensitive mechanism of the mechanical behavior of the object that drastically depends on the deformation modes. The mechanical behavior of (5, 5) NGr with empty edges under *zg* and *ach* deformation modes is similar to that of a tricotage when either the sheet rupture has both commenced and completed by the rupture of a single stitch row (*ach* mode) or the rupture of one stitch is "tugging at thread" the other stitches that are replaced by still elongated one-atom chain of carbon atoms (*zg* mode). The final equilibrium structures corresponding to the complete rupture are shown in Fig. 5.33a. To achieve the rupture, 18 and 250 steps of successive tension were needed for *ach* and *zg* modes, respectively (Sheka et al. 2011a, b).

Quite unexpectedly, the character of the deformation has occurred to be strongly dependent on chemical situation at the sheet edges (Sheka et al. 2012). As seen in Fig. 5.33b, single-H termination slightly elongates the rupture related to the *ach* mode up to the 20th step while considerably shortens the regime of the *zg* deformation mode up to the 125th step. The tricotage-like behavior of the deformation is still preserved while noticeably changes the pattern. Even more drastic changes for this mode occur when the edge atoms are double-H-terminated (Fig. 5.33c). Still, the *ach* mode is quite conservative while *zg* mode becomes practically identical to the former. The tricotage-like character of the deformation is completely lost and the rupture occurs at the 33rd step.

The observed phenomenon can be understood if suggested that (1) the deformation and rupture of the sheet is a collective event that involves the electron system of the sheet as a whole, (2) the electron system of the graphene sheet is highly delocalized and thus topologically sensitive, and (3) chemical termination of edge atoms so strongly influences the topological change of the whole sheet due to extreme correlation.

5.10 Conclusion

Discussion in this chapter has been aimed at convincing readers that sp^2 nanocarbons present a new class of topochemical objects. The novelty lies in the fact that these species demonstrate a complicated topological behavior as regards chemical reactions with their participation that manifests a combination of the inherent

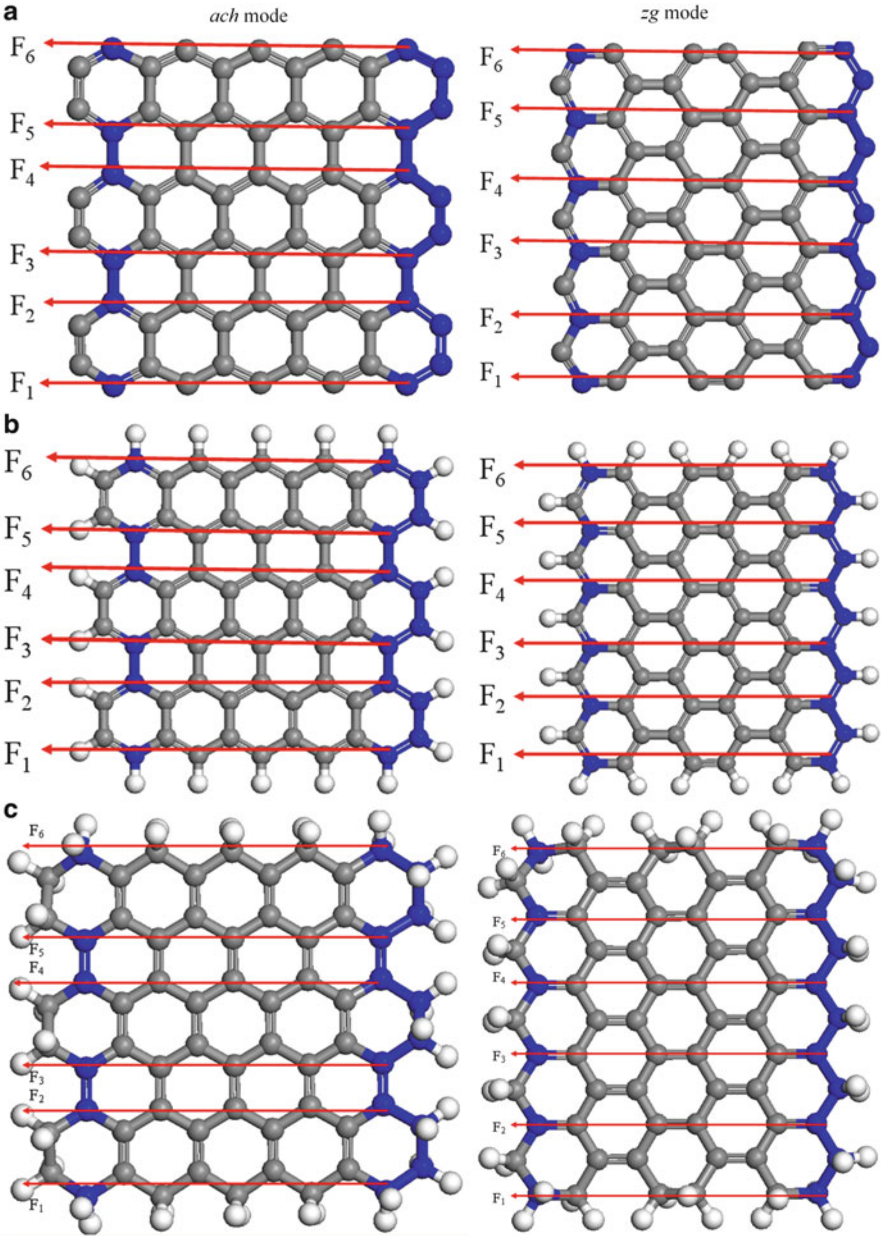

Fig. 5.32 Configurations of six mechanochemical internal coordinates related to two deformation modes of (5, 5) nanographene sheet with empty (**a**), single-H-terminated (**b**), and double-H-terminated (**c**) edge atoms. Atoms marked in *blue* are excluded from the optimization procedure (Sheka et al. 2012)

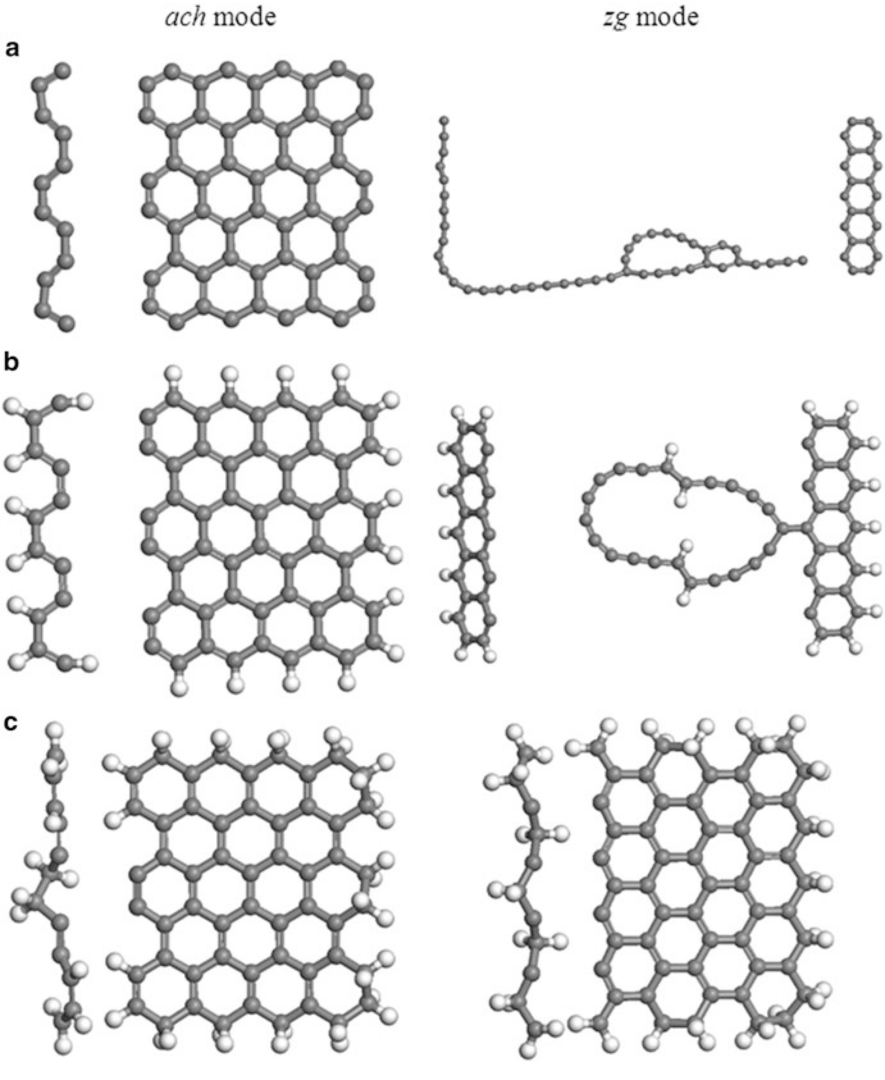

Fig. 5.33 The rupture-point final structures of (5, 5) nanographene sheet with empty (**a**), single-H-terminated (**b**), and double-H-terminated (**c**) edge atoms at two deformation modes (Sheka et al. 2012)

topology of the species, or the internal topology, with that provided by the action of external factors. The internal topology is manifested through identical reactions that involve different members of the class. Two types of such reactions have been considered, namely, the "double-(C–C)-bond" reactions between two sp^2 class members and "atom-(C–C)-bond" reactions that concern a monatomic species deposition on the sp^2 nanocarbons. The former reaction is mainly addressed to a number of composites that are formed by fullerene C_{60} attachment to either itself or carbon nanotube and nanographene. As turned out, in spite of structural similarity of the "double-(C–C)-bond" contact zones, which are mainly presented by $[2+2]$ cycloaddition junctions, the energetic parameters of the composites have revealed a deep discrepancy that manifest the different inherent topology of the species. This conclusion finds support in case of composites formed by carbon nanotubes and graphene, as well. But the brightest proof of the difference in the inherent topology of fullerenes and graphene has been obtained by comparing the hydrogenation of fullerene C_{60} and (5, 5) nanographene.

The external topological events have been demonstrated computationally by differing both structural image and energetic characteristics of (5, 5) nanographene hydrides under conditions when the pristine graphene membrane was subjected to the action of different external factors, such as immobilization of the perimeter carbon atoms, restrictions of the accessibility of both sides of the membrane, and exploring either atomic or molecular hydrogen. This finding seems to be of particular importance since it should be addressed to the chemical modification of graphene as a methodology aimed at a controllable changing of the graphene electronic properties. It is quite obvious that chemical behavior of graphene in the form of free-standing and fixed membranes, deposited layers on different substrates, in solutions and gaseous surroundings will be different. The analysis of the available experimental data gave a large support of the conclusion demonstrating, say, a sharp difference in the C_{60} fullerene oligomerization in crystalline phase, due to mechanochemical reaction in solutions, and once deposited on different substrates.

It might be thought that the revealed peculiarities of the topological behavior of sp^2 nanocarbons do not manifest its complexity in the full extent. This conclusion highlights the importance of the species consideration at the level of formal mathematical topology. It might be expected that some new faces of the phenomenon could be visualized and explained in terms of the connectivity and adjacency characteristic for the studied objects.

Meeting reproach, which might be caused by a restricted referring to studies performed by other people, it should be noted that this chapter presents the author view on the processes described. Each of the touched topics covers a large field so that the exhausted referring to what happening in the field would unavoidably make the manuscript too cumbersome. In case if some compensation may be suggested, the author publications considered in the chapter covers the situation concerning the study of each particular question quite thoroughly.

References

Boldyrev VV (1990) React Solid 8:231

Cataldo F, Graovac A, Ori O (eds) (2011) The mathematics and topology of fullerenes. Springer, New York

Chen S, Chen P, Wang Y (2011) Nanoscale 3:4323

Davydov VA, Kashevarova LS, Rakhmanina AV, Senyavin VM, Pronina OP, Oleynikov NN, Agafonov V, Céolin R, Allouchi H, Szwarc H (2001) Chem Phys Lett 333:224
de Jong AWK (1923) Ber Dtsch Chem Ges 56:818
Ecklund PC, Rao AM, Zhou P, Wang Y, Holden JM (1995) Thin Solid Film 257:185
Elias DC, Nair RR, Mohiuddin TMG, Morozov SV, Blake P, Halsall MP, Ferrari AC, Boukhvalov DW, Katsnelson MI, Geim AK, Novoselov KS (2009) Science 323:610
Enders A, Malinowski N, Ievlev D, Zurek E (2006) J Chem Phys 125:191102
Enkelmann V (1984) Adv Polym Sci 63:91
Fischer JE (1994) Science 264:1548
Friscicr̆ T, MacGillivray LR (2005) Z Kristallogr 220:351
Gao X, Zhou Z, Zhao Y, Nagase S, Zhang SB, Chen Z (2008) J Phys Chem C 112:12677
Giacalone F, Martín N (2010) Adv Mater 22:4220
Guo F, Marti-Rujas J, Pan Z, Hughes CE, Harris KDM (2008) Phys Chem C 112:19793
Haddon RC (1993) Science 261:1545
Hasegawa M (1986) Pure Appl Chem 58:1179
Hedén M, Hansen K, Campbell EEB (2005) Phys Rev A 71:055201
Iwasa Y, Arima T, Fleming RM, Siegrist T, Zhou O, Haddon RC, Rothberg LI, Lyons KB, Carter HL Jr, Hebard AF, Tycko R, Dabbagh G, Kraewski JJ, Thomas JA, Yagi T (1994) Science 264:1570
Kazaoui S, Minami N, Tanabe Y, Byrne HJ, Eilmes A, Petelenz P (1998) Phys Rev B 58:7689
Kondo D, Sato S, Awano Y (2008) Appl Phys Express 1:074003
Kunitake M, Uemura S, Ito O, Fujiwara K, Murata Y, Komatsu K (2002) Angew Chem Int Ed 41:969
Lee KH, Eun HM, Park SS, Suh YS, Jung K-W, Lee SM, Lee YH, Osawa E (2000) J Phys Chem B 104:7038
Li X, Liu L, Qin Y, Wu W, Guo Z-C, Dai L, Zhu D (2003) Chem Phys Lett 377:32
Li C, Chen Y, Wang Y, Iqbal Z, Chhowallab M, Mitra S (2007) J Mater Chem 17:2406
MacGillivray LR, Papaefstathiou GS (2004) Encyclopedia of supramolecular chemistry. Marcel Dekker, New York, p 1316. doi:10.1081/E-ESMC 120012761
Matsuo Y, Tahara K, Nakamura E (2003) Org Lett 5:3181
Merrifield RE, Simmons HE (1989) Topological methods in chemistry. Wiley, New York
Nakaya M, Kuwahara Y, Aono M, Nakayama T (2008) Small 4:538
Nakayama T, Onoe J, Nakatsuji K, Nakamura J, Takeuchi T, Aono M (1999) Surf Rev Lett 6:1073
Nasibulin AG, Anisimov AS, Pikhitsa PV, Jiang H, Brown DP, Choi M, Kauppinen EI (2007a) Chem Phys Lett 446:109
Nasibulin AG, Pikhitsa PV, Jiang H, Brown DP, Krasheninnikov AV, Anisimov AS, Queipo P, Moisala A, Gonzalez D, Lientschnig G, Hassanien A, Shandakov SD, Lolli D, Resasco DE, Choi M, Tománek D, Kauppinen EI (2007b) Nat Nanotechnol 2:156
Nikitina EA, Khavryutchenko VD, Sheka EF, Barthel H, Weis J (1999) J Phys Chem A 103:11355
Núñez-Regueiro M, Markes L, Hodeau J-L, Béthoux O, Perroux M (1995) Phys Rev Lett 74:278
Pac B, Petelenz P, Slawik M, Munn RW (1998) J Chem Phys 109:7932
Pekker S, Janossy A, Mihali L, Chauvet O, Forro L (1994) Science 265:1077
Pusztai T, Oszlányi G, Faigel G, Kamaras K, Granasy L, Pekker S (1999) Solid State Commun 111:595
Rut'kov EV, Tontegode AY, Usufov MM (1995) Phys Rev Lett 74:758
Schmidt GMJ (1971) Pure Appl Chem 27:647
Sheka EF (2004) Int J Quantum Chem 100:388
Sheka EF (2007a) Chem Phys Lett 438:119
Sheka EF (2007b) Int J Quantum Chem 107:2803
Sheka EF (2010) J Exp Theor Phys 111:395
Sheka EF (2011a) Fullerene nanoscience: nanochemistry, nanomedicine, nanophotonics, nanomagnetism. Taylor & Francis, Boca Raton
Sheka EF (2011b) J Mol Mod 17:1973
Sheka EF (2012) Int J Quantum Chem 112:3076

Sheka EF, Chernozatonskii LA (2007) J Phys Chem C 111:10771
Sheka EF, Chernozatonskii LA (2010a) J Comput Theor Nanosci 7:1814
Sheka EF, Chernozatonskii LA (2010b) Int J Quantum Chem 110:1466
Sheka EF, Chernozatonskii LA (2010c) Int J Quantum Chem 110:1938
Sheka EF, Chernozatonskii LA (2010d) J Exp Theor Phys 110:121
Sheka EF, Popova NA (2012a) arXiv:1201.1618v1 [cond-mat.mtrl-sci]
Sheka EF, Popova NA (2012b) J Mol Mod 18:3751
Sheka EF, Shaymardanova LKh (2011a) arXiv:1101.4893 [cond-mat.mes-hall]
Sheka EF, Shaymardanova LK (2011b) J Mater Chem 21:17128
Sheka EF, Zayetz VA (2005) Russ J Phys Chem 79:2009
Sheka EF, Zayetz VA, Ginzburg IY (2006) J Exp Theor Phys 103:728
Sheka EF, Razbirin BS, Starukhin AN, Nelson KD (2007) Opt Spectrosc 102:432
Sheka EF, Popova NA, Popova VA, Nikitina EA, Shaymardanova LK (2011a) J Exp Theor Phys 112:602
Sheka EF, Popova NA, Popova VA, Nikitina EA, Shaymardanova LK (2011b) J Mol Mod 17:1121
Sheka EF, Popova NA, Popova VA (2012) arXiv:1301.1895v1 [cond-mat.mtrl-sci]
Sofo JO, Chaudhari AS, Barber GD (2007) Phys Rev B 75:153401
Soldatov AV, Roth G, Dzyabchenko AV, Johnels D, Lebedkin S, Meingast C, Sundqvist B, Haluska M, Kuzmany H (2001) Science 293:680
Sun Y-P, Ma B, Bunker CE, Liu B (1995) J Am Chem Soc 117:12705
Tian Y, Chassaing D, Nasibulin AG, Ayala P, Jiang H, Anisimov AS, Kauppinen EI (2008) J Am Chem Soc 130:7188
Wang Y, Holden JM, Bi X-X, Eklund PC (1994) Chem Phys Lett 217:413
Wang X-B, Ding C-F, Wang L-S (1999) J Chem Phys 110:8217
Weaver JH, Martins JL, Komeda T, Chen Y, Ohno TR, Kroll GH, Troullier N, Haufler R, Smalley RE (1991) Phys Rev Lett 66:1741
Woodward RB, Hoffmann R (1970) The conservation of orbital symmetry. Verlag Chemie, Weinheim/Bergstr
Wu X, Zeng XC (2008) ACS Nano 2:1459
Wu X, Zeng XC (2009) Nano Lett 9:250
Yamawaki H, Yoshida M, Kakudate Y, Usuba S, Yokoi H, Fujiwara S, Aoki K, Ruoff R, Malhotra R, Lorentz D (1993) J Phys Chem 97:11161
Yan L, Zheng UB, Zhao F, Li S, Gao X, Xu B, Weiss PS, Zhao Y (2012) Chem Soc Rev 41:97
Zhang X, Tang L, Guo Q (2010) J Phys Chem C 114:6433
Zhao IB, Poirier DM, Pechman RJ, Weaver JH (1994) Appl Phys Lett 64:577